

## Benchmark solutions

## A front tracking method for particle-resolved simulation of evaporation and combustion of a fuel droplet

Muhammad Irfan<sup>a,b</sup>, Metin Muradoglu<sup>a,\*</sup><sup>a</sup> Department of Mechanical Engineering, Koc University, Rumelifeneri Yolu, Sariyer, Istanbul 34450, Turkey<sup>b</sup> Department of Mechanical Engineering, Capital University of Science and Technology, Islamabad, Pakistan

## ARTICLE INFO

## Article history:

Received 30 March 2018

Revised 25 July 2018

Accepted 14 August 2018

Available online 16 August 2018

## Keywords:

Evaporation

Combustion

Phase change

Front-tracking method

Multi-phase flows

Detailed chemistry

## ABSTRACT

A front-tracking method is developed for the particle-resolved simulations of droplet evaporation and combustion in a liquid-gas multiphase system. One field formulation of the governing equations is solved in the whole computational domain by incorporating suitable jump conditions at the interface. Both phases are assumed to be incompressible but the divergence-free velocity condition is modified to account for the phase change at the interface. A temperature gradient based evaporation model is used. An operator-splitting approach is employed to advance temperature and species mass fractions in time. The CHEMKIN package is incorporated into the solver to handle the chemical kinetics. The multiphase flow solver and the evaporation model are first validated using the benchmark problems. The method is then applied to study combustion of a n-heptane droplet using a single-step chemistry model and a reduced chemical kinetics mechanism involving 25-species and 26-reactions. The results are found to be in good agreement with the experimental data and the previous numerical simulations for the time history of the normalized droplet size, the gasification rate, the peak temperature and the ignition delay times. The initial flame diameter and the profile of the flame standoff ratio are also found to be compatible with the results in the literature. The method is finally applied to simulate a burning droplet moving due to gravity at various ambient temperatures and interesting results are observed about the flame blow-off.

© 2018 Elsevier Ltd. All rights reserved.

## 1. Introduction

The evaporation process is of fundamental importance in various natural and industrial processes. It plays a vital role to shape our atmosphere and environment, directly affecting our daily life activities. The quality of human health is also dependent on this phenomena by managing the heat content of the body. A lot of industrial applications are primarily based on the evaporation process, e.g., cooling towers, distillation plants, spray combustion to name a few. In our recent paper, a front tracking method is developed for the particle-resolved simulation of evaporation process in a multiphase system [1]. A detailed review is also presented there about the progress in the development of different modeling approaches, numerical methods and solution algorithms for the simulations of the phase change processes focusing particularly on the evaporation process.

The combustion of fuel droplets in the spray combustion is another striking application where evaporation produces fuel vapors which subsequently react with the oxidizer to form the products

of combustion. The quality of combustion is critically dependent on the atomization, the evaporation and the proper mixing and reaction of the fuel and the oxidizer. In particular, the evaporation and combustion of droplets in fuel sprays have been the area of immense interest for decades due to its industrial and defense importance. Researchers have mostly tackled this problem by studying the evaporation and combustion of a single droplet system as a base case and a first step towards the understanding of the overall spray combustion phenomena. Modeling of the evaporation process is the first step to achieve this objective for which different multiphase flow modeling techniques have been proposed in the literature. These methods include the marker and cell method [2], VOF [3], level set method [4,5], phase field method [6], diffuse interface method [7], lattice Boltzmann method [8] and front tracking method [9–11]. The front-tracking method developed by Tryggvason and coworkers [11] is a promising technique to model multi-fluid flows that has been extended by various researchers to model the phase change phenomena, e.g., evaporation and boiling [1,12–17] and solidification [12,18–21]. The front tracking method has also been successfully applied to track the flame front of a premixed flame [22], mass transfer and chemical reaction [23,24]. The front tracking method offers several advantages such as its concep-

\* Corresponding author.

E-mail address: [mmuradoglu@ku.edu.tr](mailto:mmuradoglu@ku.edu.tr) (M. Muradoglu).

tual simplicity, sharp representation of the interface, small numerical diffusion and its ability to include multi-physics effects [12]. Its main drawback is probably the difficulty to track the Lagrangian marker points and maintain communication between the Eulerian and Lagrangian grids in curvilinear and unstructured grid [72]. In addition, the topological changes are not handled automatically, rather special treatment is needed where fluid regions merge or breakup.

The pioneering study about the fuel droplet evaporation and combustion was performed in early 1950s by Godsave [25]. He examined the burning of an evaporating droplet suspended at the tip of a fine quartz fiber and interpreted his results successfully based on the assumption that the rate of burning is not controlled by the chemical reaction rates. This assumption greatly simplified the analytical treatment of the combustion of the fuel droplets. Spalding [26] conducted a detailed experimental study and showed that transfer or diffusion of mass and energy of the fuel vapor should be one of the controlling factors for the combustion process. The validity of these assumptions were critically analyzed in the later studies by numerous authors [27–33] and various advanced evaporation models were proposed [34–36]. Following these landmark studies about evaporation and combustion of droplets, the vaporization of single/multiple water, alkane and alcohol droplets have been studied experimentally by various researchers under normal or microgravity conditions [37–41]. They reported the effects of ambient pressure and temperature, convective currents and initial droplet size on the droplet equilibrium temperature, evaporation rate, droplet life time, and drag coefficient.

Various computational models and numerical techniques have been proposed in the literature to simulate the evaporation and burning of fuel droplets, and the experimental results are often used as the benchmark test cases to validate these numerical methods. Miller et al. [42] numerically evaluated different droplet evaporation models through comparisons with the experimental measurements. They observed that the constant properties assumption can be safely used in simulations provided that the properties of both the gas and the vapor phases are calculated at either the wet-bulb or boiling temperature. The literature reports the numerical studies for the evaporation and burning of *n*-heptane [43–47], decane [41,48] and methanol [49,50] droplets under various operating conditions as a first step towards the simulation of spray combustion in engine like environment. Some of the above mentioned studies are performed using the detailed transport models with the detailed chemical kinetics mechanisms and variable thermodynamic properties [44–46,49] while the others involve various simplifying assumptions such as an overall single-step irreversible reaction, constant thermodynamic properties, constant Lewis number and the ideal gas behavior [41,47,48,50]. It is argued that these simplifying assumptions are well justified to test the numerical aspects during the algorithm design and code development phase.

In this paper, a front tracking solver is developed for the particle-resolved simulations of droplet evaporation and burning. The phase change component of the method is first validated against the classic  $d^2$ -law. The method is then applied to simulate the evaporation of a *n*-heptane droplet to further validate the evaporation model and the results are found to be in good agreement with the analytical [51], the experimental [40] and the previous numerical results [43]. The phase change solver is then extended to incorporate the combustion process following the evaporation as a first step towards the development of a computational framework for the direct numerical simulations of spray combustion which is the main novelty of this article. An operator-splitting approach [52–55] is used to advance the temperature and the species mass fractions in time. The chemical kinetics in the gas phase is handled using the CHEMKIN package [56,57] in the operator-splitting framework. The method is successfully ap-

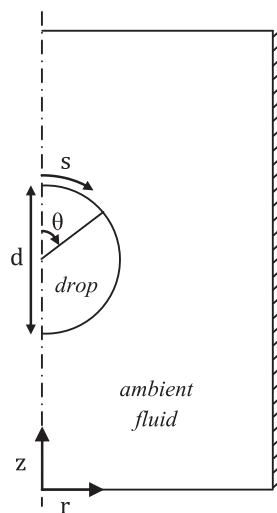


Fig. 1. The schematic illustration of a drop in an axisymmetric configuration.

plied to study the combustion of a *n*-heptane droplet using a simple single-step chemistry model and a reduced detailed chemical mechanism involving 25-species and 26-reactions. The combustion is initiated by artificially increasing the temperature locally near the droplet to ignite the fuel vapors in both the single-step and detailed chemistry simulations. It is demonstrated that, once the fuel is ignited, the combustion proceeds in a smooth fashion maintaining the spherical symmetry of the flame. The time histories of the normalized droplet size, the gasification rate and the peak temperature are found to agree well with the previous numerical results [44,58]. In addition, the ignition delay times for a burning *n*-heptane droplet are also computed and the results are found to exhibit an excellent agreement with the results of Stauch et al. [45] for different gas phase temperatures. The initial flame diameter and the profile of flame standoff ratio also verify our numerical results qualitatively. The method is finally applied to a *n*-heptane droplet falling under the action of gravity at various ambient temperature conditions. It is observed that the ambient temperature is a vital parameter that controls the flame blow-off/extinction.

The rest of the paper is organized as follows. The mathematical formulation is briefly described for an evaporating and burning droplet in a multiphase system in the next section. The numerical solution procedure is discussed in Section 3 with a particular emphasis on the treatment of the phase change and combustion. In Section 4, the numerical method is first validated using various benchmark test cases and then applied to study combustion of *n*-heptane droplet using a single-step and a detailed chemistry models. Finally, conclusions are drawn in Section 5.

## 2. Mathematical formulation

The governing equations are presented here in the framework of finite difference/front tracking (FD/FT) method. Consider an incompressible liquid-gas multiphase system in an axisymmetric configuration as shown in Fig. 1. One-field formulation of the governing equations can be used throughout the domain as long as the jumps in the property fields are properly handled across the interface and surface tension effects are taken into account appropriately [11]. Then the conservative form of the momentum conservation equations can be written for the entire computational domain as

$$\frac{\partial \rho \mathbf{u}}{\partial t} + \nabla \cdot (\rho \mathbf{u} \mathbf{u}) = -\nabla p + \rho \mathbf{g} + \nabla \cdot \mu (\nabla \mathbf{u} + \nabla \mathbf{u}^T) + \int_A \sigma \kappa \mathbf{n} \delta(\mathbf{x} - \mathbf{x}_\Gamma) dA, \quad (1)$$

where  $\mathbf{u}$  and  $\mathbf{g}$  are the velocity and the gravitational acceleration vectors, respectively,  $p$  is the pressure,  $t$  is time and  $\rho$  and  $\mu$  are the discontinuous density and viscosity fields, respectively. The last term on the right hand side represents the body force due to the surface tension, where  $\sigma$  is the surface tension coefficient,  $\kappa$  is twice the mean curvature, and  $\mathbf{n}$  is a unit vector normal to the interface. The surface tension acts only on the interface as indicated by the three-dimensional delta function  $\delta$  whose arguments  $\mathbf{x}$  and  $\mathbf{x}_\Gamma$  are the point at which the equation is being evaluated and a point at the interface, respectively.

For a multiphase system with a phase change, the incompressibility condition of the divergence-free velocity field ( $\nabla \cdot \mathbf{u} = 0$ ) does not hold at the interface where the phase change occurs. Rather, it is modified at the interface to account for the phase-change/mass-transfer, so the continuity equation becomes

$$\begin{aligned} \nabla \cdot \mathbf{u} &= \int_A (\mathbf{u}_g - \mathbf{u}_l) \cdot \mathbf{n} \delta(\mathbf{x} - \mathbf{x}_\Gamma) dA_\Gamma, \\ &= \frac{1}{h_{lg}} \left( \frac{1}{\rho_g} - \frac{1}{\rho_l} \right) \int_A \delta(\mathbf{x} - \mathbf{x}_\Gamma) \dot{q}_\Gamma dA_\Gamma, \end{aligned} \quad (2)$$

where the delta function makes the continuity equation non-zero at the interface and zero elsewhere. In Eq. (2),  $h_{lg}$  is the latent heat of vaporization and  $\dot{q}_\Gamma$  represents the heat flux per unit time at the interface. Subscripts  $\Gamma$ ,  $l$  and  $g$  represent the interface, the liquid and the gas phases of a multiphase system, respectively. Since there is a change of phase at the interface, therefore the velocity field is discontinuous and  $\mathbf{u}_g$  and  $\mathbf{u}_l$  are unequal. The difference between the velocity of the liquid and the velocity of vapor is related to the evaporation rate ( $\dot{m}_\Gamma$ ) and the velocity of the phase boundary ( $\mathbf{u}_\Gamma$ ) through the mass jump condition given below. The discontinuous velocity field is incorporated into Eq. (1) while solving the Poisson equation for the pressure field in the projection method. The mass and momentum jump conditions at the interface are

$$\rho_l (\mathbf{u}_l - \mathbf{u}_\Gamma) \cdot \mathbf{n} = \rho_g (\mathbf{u}_g - \mathbf{u}_\Gamma) \cdot \mathbf{n} = \dot{m}_\Gamma, \quad (3)$$

$$\dot{m}_\Gamma (\mathbf{u}_g - \mathbf{u}_l) = (\boldsymbol{\tau}_g - \boldsymbol{\tau}_l) \cdot \mathbf{n} - (p_g - p_l) \mathbf{n} + \sigma \kappa \mathbf{n}, \quad (4)$$

where  $\dot{m}_\Gamma$  is the mass flux per unit time across the interface and  $\boldsymbol{\tau}$  is the viscous stress tensor.

The energy equation can be written for the whole domain by incorporating the effects of phase change and chemical reaction and is given by

$$\begin{aligned} \frac{\partial \rho c_p T}{\partial t} + \nabla \cdot \rho c_p T \mathbf{u} &= \nabla \cdot k \nabla T - \Lambda \int_A \delta(\mathbf{x} - \mathbf{x}_\Gamma) \dot{q}_\Gamma dA_\Gamma \\ &+ \sum_{\alpha=1}^{n_s} \dot{\Omega}_\alpha H_\alpha(T), \end{aligned} \quad (5)$$

where  $T$  is the temperature,  $c_p$  is the specific heat at constant pressure and  $k$  is the thermal conductivity. The second term on the right hand side incorporates the thermal effects of phase change into the energy equation where the coefficient  $\Lambda = (1 - (c_{p,g} - c_{p,l})T_{sat}/h_{lg})$  is a constant which modifies the latent heat  $h_{lg}$  due to unequal specific heats of the liquid and gas phases. Subscript  $sat$  denotes the saturation value of the variable. The last term in Eq. (5) represents the total heat source as a result of chemical reaction, where  $\dot{\Omega}_\alpha$  represents the production rate of  $\rho Y_\alpha$  as a result of chemical reactions and  $H_\alpha(T)$  represents the enthalpy of the species component  $\alpha$ .  $Y_\alpha$  is the mass fraction of the species component  $\alpha$  and  $n_s$  is the total number of species in the system.

The species mass fraction  $Y_\alpha$  evolves in the whole domain ac-

cording to the following convection-diffusion equation

$$\begin{aligned} \frac{\partial \rho Y_\alpha}{\partial t} + \nabla \cdot \rho Y_\alpha \mathbf{u} &= \nabla \cdot \rho D_\alpha \nabla Y_\alpha + \dot{S}_\alpha + \dot{\Omega}_\alpha, \\ \alpha &= 1, 2, \dots, n_s, \end{aligned} \quad (6)$$

where  $D_\alpha$  is the mass diffusion coefficient and  $\dot{S}_\alpha$  is the production rate due to evaporation of the species component  $\alpha$ . In the present study, a single component fuel droplet is considered so  $\dot{S}_\alpha$  would be valid for fuel only (denoted by  $\dot{S}_F$ ) whereas  $\dot{\Omega}_\alpha$  involves all the species involved in the chemical reaction. Species equation is solved in the gas domain outside the liquid droplet for all the species involved in the chemical reaction.

The energy and species jump conditions must be satisfied to ensure the energy and mass conservation across the interface. These are:

$$\dot{m}_\Gamma h_{lg} = \dot{q}_\Gamma = k_g \left. \frac{\partial T}{\partial n} \right|_g - k_l \left. \frac{\partial T}{\partial n} \right|_l, \quad (7)$$

$$\dot{m}_\Gamma Y_l^\Gamma - \dot{m}_\Gamma Y_g^\Gamma + \rho_g D_\alpha \left. \frac{\partial Y}{\partial n} \right|_\Gamma = 0. \quad (8)$$

The chemical kinetics is briefly described here only for a single-step mechanism without loss of generality since it includes all the essential ingredients as far as the numerical method is concerned. The overall reaction for the oxidation of a fuel can be expressed by the following global reaction mechanism



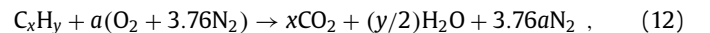
where one mole of fuel reacts with  $a$  moles of oxidizer to produce  $b$  moles of products. The oxidizer is air which is assumed to be composed of 21%  $O_2$  and 79%  $N_2$  (by volume), i.e., for each mole of  $O_2$  in air, there are 3.76 moles of  $N_2$ . For a global reaction given by Eq. (9), the rate of fuel consumption can be expressed as [51]

$$\frac{d[X_F]}{dt} = -G(T)[X_F]^n[X_{Ox}]^m, \quad (10)$$

where  $[X_i]$  denotes the molar concentration of the  $i$ th species in the mixture and  $G$  is the global rate coefficient which is a strong function of temperature  $T$ . The minus sign indicates that the fuel concentration decreases with time. Molecular collision theory can be used to derive an expression for the rate coefficient for bimolecular reactions. If the temperature range of interest is not too great, the bimolecular rate coefficient can be expressed by the empirical Arrhenius form as

$$G(T) = A \exp(-E_A/RT), \quad (11)$$

where  $A$  is a constant called the pre-exponential factor or the frequency factor,  $E_A$  is the activation energy and  $R$  is the general gas constant [51]. For a hydrocarbon fuel  $C_xH_y$ , the stoichiometric relation can be written as



where

$$a = x + y/4. \quad (13)$$

In general, the chemical kinetics is expressed in terms of ordinary differential equations (ODEs). The main difficulty arises from the fact that the ODEs are highly non-linear and extremely stiff.

Finally, we assume that the material properties remain constant following a fluid particle, i.e.,

$$\frac{D\rho}{Dt} = 0; \quad \frac{D\mu}{Dt} = 0; \quad \frac{Dk}{Dt} = 0; \quad \frac{Dc_p}{Dt} = 0; \quad \frac{DD_\alpha}{Dt} = 0, \quad (14)$$

where  $\frac{D}{Dt} = \frac{\partial}{\partial t} + \mathbf{u} \cdot \nabla$  is the material derivative.

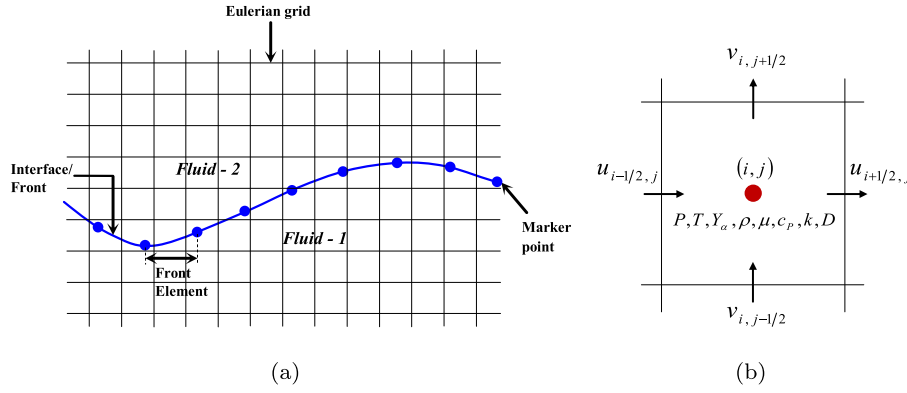


**Fig. 2.** (a) The schematic illustration of an interface on an Eulerian mesh. (b) The staggered grid used for the solution of the governing equations. The location of the storage of the flow field variables and material properties are also shown.

The governing equations are solved in their dimensional forms however some results are presented in terms of the non-dimensional quantities. The relevant non-dimensional parameters for this study can be expressed as

$$\gamma = \frac{\rho_l}{\rho_g}; \quad \zeta = \frac{\mu_l}{\mu_g}; \quad Sc = \frac{\mu_g}{\rho_g D_\alpha}; \quad Pr = \frac{\mu c_p}{k};$$

$$Re = \frac{\rho_g u_s l_s}{\mu_g}; \quad St = \frac{c_{p,g}(T_\infty - T_{sat})}{h_{lg}}, \quad (15)$$

where  $\gamma$  and  $\zeta$  represent the density and the viscosity ratios, respectively.  $Sc$ ,  $Pr$ ,  $Re$  and  $St$  are the Schmidt number, the Prandtl number, the Reynolds number and the Stefan number, respectively. Note that  $u_s$  and  $l_s$  in Eq. (15) are appropriately selected velocity and length scales, respectively, and  $t_s = l_s/u_s$  be the time scale.

### 3. Numerical solution procedure

The flow equations are solved fully coupled with the energy and the species conservation equations on a uniform, Eulerian, staggered MAC grid using a finite-difference/front-tracking method [11–14,59]. In this method, the interface (or front) is represented by connected Lagrangian marker points and is tracked explicitly [11,12,59]. Each marker point moves with the local flow velocity interpolated from the neighboring stationary regular Cartesian Eulerian grid, in addition to the velocity induced by the phase change, Eq. (18) and (19). A piece of the interface between two adjacent marker points is called a front element. The schematic representation of the Lagrangian grid on the background Eulerian mesh is shown in Fig. 2(a). The pressure, temperature, species mass fractions and all material properties are stored at the cell centers, whereas, the velocity components are stored at the cell face centers on an Eulerian grid (Fig. 2(b)).

The Indicator function  $I(\mathbf{x}, t)$  tracks different phases of a multiphase system in the computational domain both in space and time, and is defined as:

$$I(\mathbf{x}, t) = \begin{cases} 1 & \text{in droplet phase,} \\ 0 & \text{in bulk phase.} \end{cases} \quad (16)$$

The indicator function  $I(\mathbf{x}, t)$  is computed at each time step using the standard procedure as described in detail by Tryggvason et al. [12,59], which involves solution of a separable Poisson equation. The material property fields are then updated at each time step as a function of indicator function  $I(\mathbf{x}, t)$  as follows

$$\rho = \rho_l I(\mathbf{x}, t) + \rho_g (1 - I(\mathbf{x}, t));$$

$$\mu = \mu_l I(\mathbf{x}, t) + \mu_g (1 - I(\mathbf{x}, t));$$

$$k = k_l I(\mathbf{x}, t) + k_g (1 - I(\mathbf{x}, t));$$

$$\rho c_p = \rho_l c_{p,l} I(\mathbf{x}, t) + \rho_g c_{p,g} (1 - I(\mathbf{x}, t));$$

$$D_\alpha = D_{\alpha,g} (1 - I(\mathbf{x}, t)). \quad (17)$$

Surface tension forces as well as heat and mass fluxes are calculated at the Lagrangian interface. These quantities are required on the Eulerian grid while solving the momentum, energy and species conservation equations, respectively. Likewise, the velocities are available at the Eulerian grid and we need them at the Lagrangian marker points for the advection of the interface. This communication between the background Eulerian mesh and the Lagrangian interface is performed in a conservative manner using Peskin's distribution function [60]. The details of this mechanism in the framework of FD/FT method can be found in the literature [11,12,59]. The standard symmetric Peskin's distribution function is modified for implementing the fuel vapor mass fraction boundary condition at the interface as discussed in Section 3.4.

The interface is moved by updating the location of the marker points at each time step. The interface marker points move with the velocity interpolated from the Eulerian grid as well as the velocity due to the phase change as given below

$$\frac{d\mathbf{x}_\Gamma}{dt} = u_n \mathbf{n}_\Gamma, \quad (18)$$

where

$$u_n = \frac{1}{2} (\mathbf{u}_l + \mathbf{u}_g) \cdot \mathbf{n} - \frac{q_\Gamma}{2h_{lg}} \left( \frac{1}{\rho_l} + \frac{1}{\rho_g} \right). \quad (19)$$

In Eq. (19),  $\mathbf{u}_l$  and  $\mathbf{u}_g$  are the liquid and gas phase velocities, respectively, evaluated at the interface using one sided interpolation. The interface restructuring is also performed at each time step to keep it smooth and within the prescribed resolution limits. The finite-difference/front-tracking method for a multiphase system including the effects of phase change has been discussed in details by various authors [1,11–15,59]. The flow and phase change solvers are briefly described here for the sake of completeness and the continuity of the article. Emphasis is placed on the chemical kinetics solver and its coupling with the multiphase phase solver, which is the main novelty of this article.

#### 3.1. Flow solver

The flow equations are solved on a staggered Eulerian grid. The spatial derivatives are discretized using a second-order central differences for all the field quantities except for the convective terms for which a third-order QUICK scheme [61] is used. The time integration is performed using a projection method proposed by Chorin [62]. Following Unverdi and Tryggvason [11], the momentum equations can be written in the form:

$$\frac{\rho^{n+1} \mathbf{u}^{n+1} - \rho^n \mathbf{u}^n}{\Delta t} = \mathbf{A}^n - \nabla p, \quad (20)$$

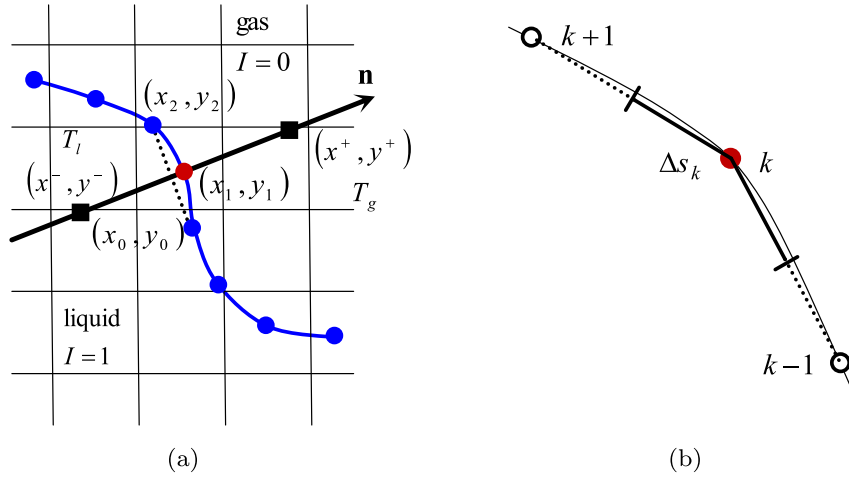


**Fig. 3.** (a) The schematic diagram illustrating the computation of  $T_g$ ,  $T_l$  and the temperature gradient for the  $k$ th marker point of the interface. (b) Computation of the interface length  $\Delta s_k$  corresponding to the  $k$ th marker point.

where  $\mathbf{A}$  represents the advection, diffusion, gravitational and the surface tension force terms. Superscript  $n$  indicates the current time level. The projection method decomposes the above equation as

$$\frac{\rho^{n+1}\mathbf{u}^* - \rho^n\mathbf{u}^n}{\Delta t} = \mathbf{A}^n, \quad (21)$$

$$\frac{\rho^{n+1}\mathbf{u}^{n+1} - \rho^{n+1}\mathbf{u}^*}{\Delta t} = -\nabla p, \quad (22)$$

where  $\mathbf{u}^*$  is the unprojected velocity field obtained from Eq. (21) by ignoring the effects of pressure. To solve for the pressure field, we take divergence of Eq. (22) to obtain a non-separable Poisson equation for the pressure, i.e.,

$$\nabla \cdot \frac{1}{\rho^{n+1}} \nabla p = \frac{\nabla \cdot \mathbf{u}^* - \nabla \cdot \mathbf{u}^{n+1}}{\Delta t}. \quad (23)$$

For  $\nabla \cdot \mathbf{u}^{n+1}$ , we use Eq. (2) as

$$\nabla \cdot \mathbf{u}^{n+1} = \frac{1}{h_{lg}} \left( \frac{1}{\rho_g} - \frac{1}{\rho_l} \right) \left[ \int_A \delta(\mathbf{x} - \mathbf{x}_\Gamma) \dot{q}_\Gamma dA_\Gamma \right]^{n+1}, \quad (24)$$

where  $\dot{q}_\Gamma$  is computed at  $(n+1)$  time level. We substitute Eq. (24) into Eq. (23) and solve the resulting Poisson equation for pressure using the multigrid solver MUDPACK [63] as described by Tryggvason et al. [12]. Finally the velocity field at the next time level,  $\mathbf{u}^{n+1}$ , is computed using Eq. (22) as:

$$\mathbf{u}^{n+1} = \mathbf{u}^* - \frac{\Delta t}{\rho^{n+1}} \nabla p. \quad (25)$$

The above algorithm is first order accurate in time. However, it can easily be extended to achieve a formally second-order accuracy using a predictor corrector scheme as described by Tryggvason et al. [12,14]. The first order method is employed here because the temporal discretization error is generally found to be negligibly small compared to the spatial error mainly due to a small time step imposed by the numerical stability of the present explicit scheme.

### 3.2. Temperature gradient based evaporation model

Referring Fig. 3, the heat flux per unit time across the  $k$ th marker point of the interface is computed by applying the energy jump condition (Eq. (7)) as

$$\dot{q}_{\Gamma_k} = k_g \frac{\partial T}{\partial n} \Big|_g^{\Gamma_k} - k_l \frac{\partial T}{\partial n} \Big|_l^{\Gamma_k}, \quad (26)$$

where  $\Gamma_k$  represents the  $k$ th marker point of the interface. A first-order accurate one-sided finite difference discretization of Eq. (26) yields [14,64]

$$\dot{q}_{\Gamma_k} = \frac{1}{\eta h} [k_g(T_g - T_{sat}) - k_l(T_{sat} - T_l)], \quad (27)$$

where  $T_g$  and  $T_l$  are the temperatures approximated at points  $(x^+, y^+)$  and  $(x^-, y^-)$  using a bi-linear interpolation, as shown in Fig. 3(a). These points are at a distance  $\eta h$ , normal from the  $k$ th marker point  $(x_1, y_1)$ . In Eq. (27),  $h$  is the uniform grid spacing and  $\eta$  scales the length of the probe and can be selected between 1 and 2 without any significant effect on the results [14,15,18]. For the current study  $\eta = 2$ .

Having found  $\dot{q}_{\Gamma_k}$ , the evaporative energy source term, i.e., the second term on the right hand side of Eq. (5), is first evaluated at the interface and then smoothed onto the neighboring fixed grid nodes in a conservative manner. Following Tryggvason et al. [12,59], for smoothing an interface quantity, say  $\phi_\Gamma$ , onto fixed grid node  $(i, j)$  in two-dimensions, we must have

$$\int_{\Delta s} \phi_\Gamma(s) ds = \int_{\Delta A} \phi_{i,j}(\mathbf{x}) dA, \quad (28)$$

which is approximated for an axisymmetric configuration as

$$\phi_{i,j} = \sum_k \phi_\Gamma^k w_{i,j}^k \frac{r_k \Delta s_k}{r_{i,j} h^2}, \quad (29)$$

where  $r_k$  and  $r_{i,j}$  are the radial coordinates of the  $k$ th marker point and the grid node  $(i, j)$ , respectively,  $\Delta s_k$  is the length of the piece of the interface between the centers of the front elements sharing the  $k$ th marker point and is calculated as shown by the thick lines in Fig. 3(b), and  $w_{i,j}^k$  is the weight of the fixed grid node  $(i, j)$  corresponding to the  $k$ th marker point and is calculated using the Peskin's cosine function [60]. The weights must also satisfy the consistency condition

$$\sum_{i,j} w_{i,j}^k = 1. \quad (30)$$

To find the evaporation source term representing the production of fuel vapors,  $\dot{S}_F$ , the evaporation mass flux per unit time  $\dot{m}_{\Gamma_k}$  is needed which is calculated as

$$\dot{m}_{\Gamma_k} = \frac{\dot{q}_{\Gamma_k}}{h_{lg}}. \quad (31)$$



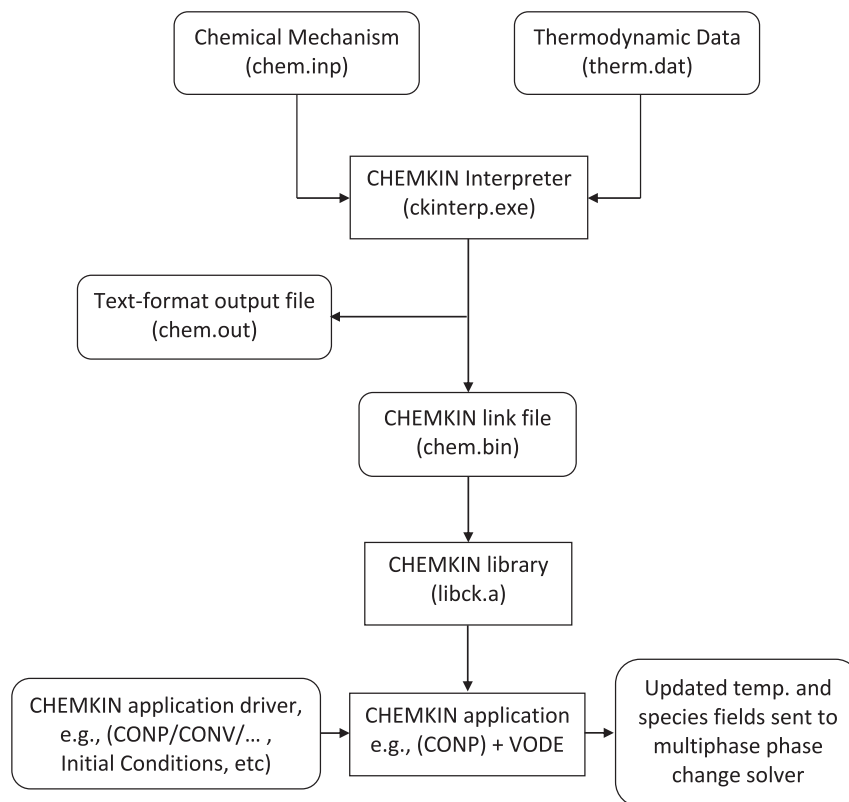


Fig. 4. Block diagram illustrating the general flow of information in CHEMKIN and its relationship to an application program.

### 3.3. Combustion of an evaporating fuel droplet

Combustion of a fuel droplet involves a large number of highly non-linear chemical reactions with a wide range of time scales making the chemical kinetic equations notoriously stiff. CHEMKIN [56,57] is a powerful tool to incorporate the gas-phase chemical kinetics into the fluid dynamics simulations. CHEMKIN, in combination with a general-purpose stiff ordinary differential equation integration package, VODE [65], is used to simulate the burning of fuel vapors in air produced as a result of evaporation of fuel droplet. Information about elements, species, chemical reaction mechanism and thermodynamic data is required as an input. This information is provided using two input files: *chem.inp* and *therm.dat*. The CHEMKIN interpreter reads this symbolic information and create two output files: *chem.bin* and *chem.out*. The *chem.bin* file is a binary linking file containing the information on the chemical elements, species, reactions and thermodynamic data extracted from the *chem.inp* and *therm.dat* whereas *chem.out* is a text-format output of the interpreter containing all the details related to chemical reaction and an information about any error occurred while generating the binary linking file. *chem.bin* is then used in combination with the CHEMKIN library, VODE, and a driver file specifying the type of problem and the relevant initial conditions to solve the problem for the desired output data, e.g., the temperature and species fields in our case. A general structure of the CHEMKIN package is shown in Fig. 4.

The whole set of governing equations are solved coupled with the gas-phase chemical kinetics. The continuity condition, Eq. (2), must be satisfied during the process. The Navier–Stokes equations are solved as explained in Section 3.1. The solution of the energy and species equations is advanced in time using a splitting scheme [52,55] that computationally decouples the chemistry and the CFD components. The chemistry part is first solved for the evolution of

the species and temperature fields in the domain from  $t^n$  to  $t^{n+1}$

$$\frac{\partial \rho c_p T}{\partial t} = \sum_{\alpha=1}^{n_s} \dot{\Omega}_\alpha H_\alpha(T), \quad (32)$$

$$\frac{\partial \rho Y_\alpha}{\partial t} = \dot{\Omega}_\alpha \quad \alpha = 1, 2, \dots, n_s. \quad (33)$$

This step is performed using CHEMKIN in combination with VODE [65]. VODE uses time-implicit backward difference methods to integrate the chemistry component and utilizes adaptivity in the order of accuracy and sub-cycled time-step selection so that an absolute error tolerance of  $10^{-16}$  in mass fractions is maintained throughout [52]. In the second step, the CFD components of the energy and species equations are advanced in time using an explicit Euler method. All spatial derivatives in the energy and species equations are approximated using second-order central differences except for the convective terms where a 5th order WENO-Z [66] scheme is used. This splitting scheme is first order accurate and is consistent with accuracy of the overall solution procedure.

### 3.4. Boundary conditions at the interface

Temperature is specified as the Dirichlet boundary condition at the interface following the procedure described by Gibou et al. [67] and Sato and Niceno [68]. For the implementation of fuel mass fraction boundary condition at the interface, two different approaches are discussed in our previous article [1]. It was concluded that the strategy that adds the evaporation mass flux as a source term to the species equation, following the adsorption layer concept developed by Muradoglu and Tryggvason [69,70] for treating soluble surfactant, is easy to implement, is numerically efficient and yields better results as compared to the one that imposes the species mass fraction at the interface directly as the Dirichlet

boundary condition [67,68]. So the fuel vapors produced at the interface due to evaporation are distributed onto the fixed grid following the adsorption layer concept of Muradoglu and Tryggvason. This constitutes the evaporative source term for the fuel vapor mass fraction  $\dot{S}_F$  in Eq. (6). The procedure is briefly described here. The evaporative source term  $\dot{S}_{\alpha i,j}$  ( $\dot{S}_{F i,j}$  for fuel vapors) at grid node  $(i, j)$  is approximated as [12,59]

$$\dot{S}_{\alpha i,j} = \sum_k \dot{m}_{\Gamma_k} w_{i,j}^k \frac{r_k \Delta s_k}{r_{i,j} h^2}, \quad (34)$$

where the weight should satisfy the consistency condition, Eq. (30), in order to conserve the total source strength in going from the interface to the grid. The weight for the grid node  $(i, j)$ , for smoothing a quantity from the  $k$ th marker point, can be written as

$$w_{i,j}^k = \frac{\tilde{w}_{i,j}^k}{\sum_i \sum_j \tilde{w}_{i,j}^k}. \quad (35)$$

The non-normalized weight is obtained as a product of one-dimensional distribution functions, i.e.,

$$\tilde{w}_{i,j}^k = \Psi(x_{\Gamma_k} - ih) \Psi(y_{\Gamma_k} - jh), \quad (36)$$

where  $(x_{\Gamma_k}, y_{\Gamma_k})$  is the coordinate of the  $k$ th marker point and the distribution function  $\Psi$  is a slightly modified version of the Peskin's cosine function [60,69,70] defined as

$$\Psi(x) = \begin{cases} \frac{1}{2\lambda} (1 + \cos(\frac{\pi x}{\lambda})) & \text{if } |x| < \lambda \text{ and } I < 0.5, \\ 0 & \text{otherwise,} \end{cases} \quad (37)$$

where  $\lambda$  is the width of the layer onto which  $\dot{m}_{\Gamma_k}$  is distributed as a mass source, and is selected as  $\lambda = 2h$  in the present study. We also checked for  $\lambda = 3h$  but no considerable effect on the output parameters is observed.

### 3.5. Overall solution procedure

The overall solution procedure is briefly outlined below:

- Heat and mass fluxes per unit time for the marker points,  $\dot{q}_{\Gamma}^n$  and  $\dot{m}_{\Gamma}^n$ , are computed using temperature and species fields at time level  $n$ , using Eq. (27) and Eq. (31), respectively.
- $\dot{q}_{\Gamma}^n$  is distributed onto the fixed grid using the Peskin's distribution function [60].
- The procedure described in Section 3.4 is used to handle the species mass fraction boundary condition at the interface.
- Interface is advected and the coordinates of marker points for the next time level,  $n + 1$ , are obtained by integrating Eq. (18) as  $\mathbf{x}_{\Gamma}^{n+1} = \mathbf{x}_{\Gamma}^n + \Delta t (u_n \mathbf{n}_{\Gamma})^n$ , where  $u_n$  is computed using Eq. (19).
- Indicator function  $I^{n+1}$  is computed based on the new interface location,  $\mathbf{x}_{\Gamma}^{n+1}$ . Then  $(\rho c_p)^{n+1}$  field is evaluated based on the updated indicator function of  $I^{n+1}$ .
- The CHEMKIN solver is triggered at this stage to solve the chemical kinetic mechanism for a particular chemical reaction in combination with the VODE and Eqs. ((32) and (33)) using the temperature and species fields of the time level  $n$ . The output of this step is the updated temperature and species fields that will subsequently be used while solving the energy and species equations for the time level  $n + 1$ .
- The CFD components of the energy (Eq. (5)) and species (Eq. (6)) equations are then solved for the updated temperature  $T^{n+1}$  and species  $Y^{n+1}$  fields, respectively.
- $\dot{q}_{\Gamma}^{n+1}$  is calculated for the time level  $n + 1$  and distributed onto the fixed grid following the steps i - ii.
- Next, the flow equations are solved for the new velocity field,  $\mathbf{u}^{n+1}$ , as discussed in Section 3.1. We need the surface tension term while solving the Navier–Stokes equations.

We compute the surface tension for each front element at time level  $n$  and distribute it onto the neighboring fixed grid nodes using the Peskin's distribution function [60].

- The material property fields are updated for the time level  $n + 1$  using Eq. (17).
- The Lagrangian interface grid is restructured at each time step to keep the interface smooth and the front element size within the prespecified limits.

## 4. Results and discussion

### 4.1. Axisymmetric multiphase solver

This section aims to validate the front tracking multiphase solver in an axisymmetric configuration. A section of the droplet is actually simulated by exploiting the axisymmetry condition along the  $z$ -axis. The set of governing equations, (Eqs. (1), (5) and (6)), are used with  $\dot{q}_{\Gamma} = \dot{S}_{\alpha} = \dot{\Omega}_{\alpha} = 0$  in combination with the incompressibility condition  $\nabla \cdot \mathbf{u} = 0$  satisfied throughout the domain.

The validation case simulates the gravity driven falling droplet in a straight channel for which numerical results are available in the literature [71,72]. An initially spherical liquid droplet of diameter  $d$  is centered at  $(r_c, z_c) = (0, 13.75d)$  in a rigid cylinder filled with an ambient fluid. Due to higher density of the droplet as compared to the ambient fluid, the droplet accelerates downwards. The computational domain is  $5d$  and  $15d$  in the radial and axial directions, respectively. At the cylinder walls no-slip boundary conditions are applied whereas the axisymmetry conditions are applied at the centerline. The problem is governed by four non-dimensional parameters, namely, the Eötvös number  $Eo = g_z (\rho_d - \rho_o) d^2 / \sigma$ , the Ohnesorge number  $Oh_d = \mu_d / \sqrt{\rho_d d \sigma}$ , the density ratio  $\gamma = \rho_d / \rho_o$  and the viscosity ratio  $\zeta = \mu_d / \mu_o$ . The Ohnesorge number for the ambient fluid is defined as  $Oh_o = \mu_o / \sqrt{\rho_o d \sigma}$ . The subscripts 'd' and 'o' denote the properties of drop and ambient fluids, respectively. The computational domain is resolved by a  $512 \times 1536$  uniform Cartesian grid. For all the results presented here, the physical properties are selected to have the non-dimensional parameters as:  $Oh_d = 0.0466$ ,  $Oh_o = 0.05$ ,  $\gamma = 1.15$  and  $\zeta = 1$ . The axial component of the gravitational acceleration,  $g_z$ , is varied to achieve the desired  $Eo$  numbers as 12, 24, 48 and 96. The time and centroid velocity are non-dimensionalized by the time scale  $\sqrt{d/g_z}$  and the velocity scale  $\sqrt{dg_z}$ , respectively. First, the results are presented for the shape evolution of the droplet as it moves down the channel for  $Eo = 48$  and 96. The qualitative comparison with the results of Han and Tryggvason [71] shows excellent agreement with some minor discrepancies as shown in Fig. 5. Next, the comparison is made for the non-dimensional centroid velocity  $V^*$  of the falling droplet as shown in Fig. 6. An excellent quantitative agreement is also observed with the results of Han and Tryggvason [71] for  $Eo = 12$  and 24. However, some deviations are seen for higher  $Eo$  numbers, which are mainly due to the fact that the drop shape is deformed substantially as  $Eo$  increases and in certain regions numerical resolution is not good enough to capture the full physics of the problem. Also, the numerical approximations and the restructuring of the interface for highly deformed geometry may have contributed towards these deviations. The volume conservation error is also plotted in Fig. 6. As can be seen, the error is less than 0.2% for all the studied cases.

### 4.2. Temperature gradient based phase change

After validating the multiphase solver, the temperature gradient based phase change process is incorporated into the numerical method as described in Section 4.1. The governing equations, Eqs. ((1), (5) and (6)), are solved in combination with the modified continuity equation, Eq. (2), in the front tracking framework.

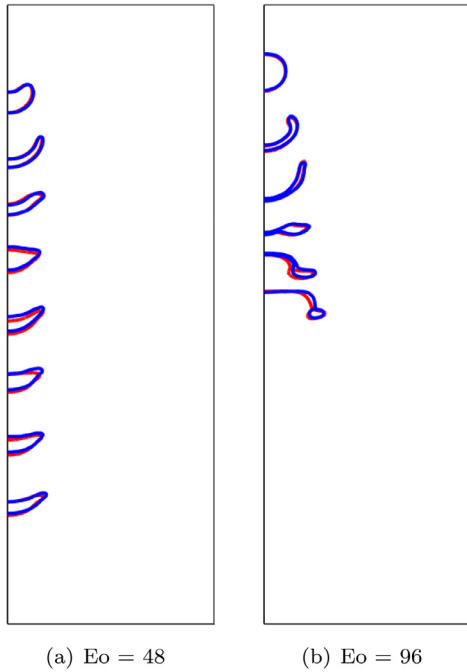


**Fig. 5.** Comparison of the present results (blue) with the numerical results of Han and Tryggvason [71] (red) for the evolution of drop shapes as it moves down the channel under the gravitational force for Eötvös numbers (a)  $Eo = 48$  and (b)  $Eo = 96$ . The other non-dimensional parameters are  $Oh_d = 0.0466$ ,  $Oh_o = 0.05$ ,  $\gamma = 1.15$  and  $\zeta = 1$ . The first and last interfaces are plotted for case (a) at  $t^* = 5.59$  and  $44.72$ , and for case (b) at  $t^* = 3.162$  and  $34.78$ . The gap between two successive drops in each column represents the distance the drop travels at a fixed time interval. Grid:  $512 \times 1536$ . (For interpretation of the references to color in this figure legend, the reader is referred to the web version of this article.)

In this section, chemical reaction is not yet included, therefore,  $\dot{\Omega}_\alpha$  is set to 0 in Eqs. (5) and (6). Numerical implementation details particular to this process are explained in Section 3.2.

#### 4.2.1. Validation test - $d^2$ -law

This case simulates a static liquid droplet of initial diameter  $d_o$  evaporating in a hot gaseous environment. An axisymmetric droplet is centered at  $(0, 5d_o)$  in a domain of size  $5d_o$  and  $10d_o$  in the radial and axial directions, respectively, as sketched in Fig. 1. The domain is discretized using  $256 \times 512$  uniform grid cells. The temperature of the droplet is initialized as  $T_{sat}$  and stays fixed

during the whole simulation, whereas the gas phase temperature is initialized as  $T_g$  which evolves as the simulation proceeds. The same initial gas phase temperature is set as the wall temperature boundary condition. At the interface,  $T_{sat}$  is applied as the Dirichlet interface temperature boundary condition following the strategy discussed in Section 3.4 [67,68]. The length and time scales are selected as  $d_o$  and  $d_o^2/\alpha_g$ , respectively, where  $\alpha_g$  is the thermal diffusivity of the gaseous phase.

Numerical results are presented and compared with the analytical solution for the variation of normalized  $d^2$  with the non-dimensional time  $t^*$  for various Stefan numbers. The analytical solution is available in the combustion textbooks [51,73] for this classical phase change problem, termed as  $d^2$ -law, and is expressed as

$$\frac{dd^2}{dt} = -\frac{8k_g}{\rho_l c_{p,g}} \ln(1 + St). \quad (38)$$

The numerical and analytical results match very well for all the studied cases as shown in Fig. 7(a). However, a slight difference exists between the slopes of the analytical and the numerical results. One striking reason for this difference is the fact that as the droplet gets smaller and smaller, grid resolution of the droplet gets worse and results deviate from the analytical solution. Second, in the analytical solution it is assumed that droplet evaporates in an infinite domain whereas, in numerical simulations, the computational cost restricts the domain dimensions to a finite size. We numerically experimented with different domain sizes for  $St = 0.025$ ; the numerical results approach the analytical solution as we increase the domain size, as shown in Fig. 7(b). Another reason may be the volume conservation error (negative error in our case) associated with the front tracking solver itself, as shown in Fig. 6. This supports and is consistent with the slightly higher slopes in the numerical results. The results are expected to be further improved by grid refinement and by using stretched grid or adaptive mesh refinement.

Next, the results are presented for a *n*-heptane droplet evaporating in a quiescent nitrogen environment. This case is studied experimentally by Nomura et al. [40] in a microgravity environment, and has been used by various researchers as a benchmark case to validate their phase change solvers [43]. Fig. 8 shows the results of the normalized  $d^2$  variation with  $t/d_o^2$  where  $d_o$  is the initial drop diameter. Two separate cases are studied with different initial gas phase temperatures  $T_g$ . The domain size is  $2.5d_o$  and  $5d_o$  in the radial and axial directions, respectively, and resolved by  $192 \times 384$  uniform grid cells. The temperature inside the droplet is initialized

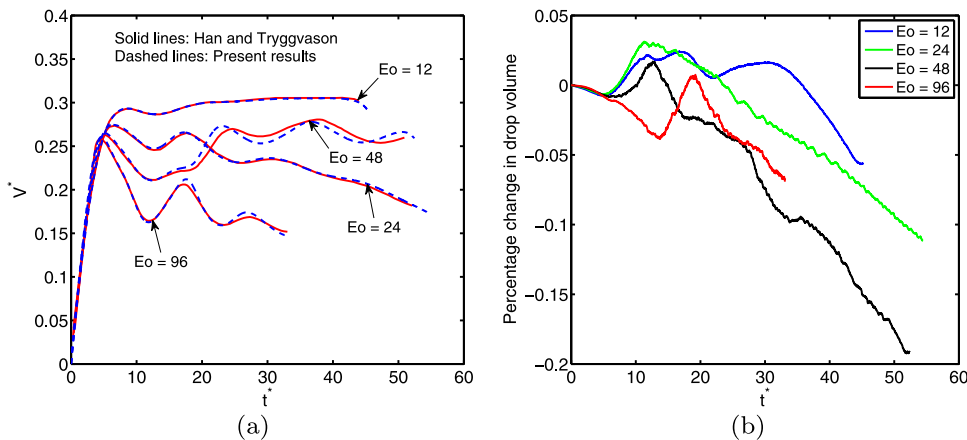


**Fig. 6.** (a) Comparison of the non-dimensional centroid velocity  $V^*$  of a falling droplet with the numerical results of Han and Tryggvason [71] for  $Eo = 12, 24, 48$  and  $96$ . (b) The volume conservation error is plotted against the non-dimensional time  $t^*$ . The error is less than 0.2% for all the cases. The non-dimensional parameters for this study are  $Oh_d = 0.0466$ ,  $Oh_o = 0.05$ ,  $\gamma = 1.15$  and  $\zeta = 1$ . Grid:  $512 \times 1536$ . (For interpretation of the references to color in this figure legend, the reader is referred to the web version of this article.)



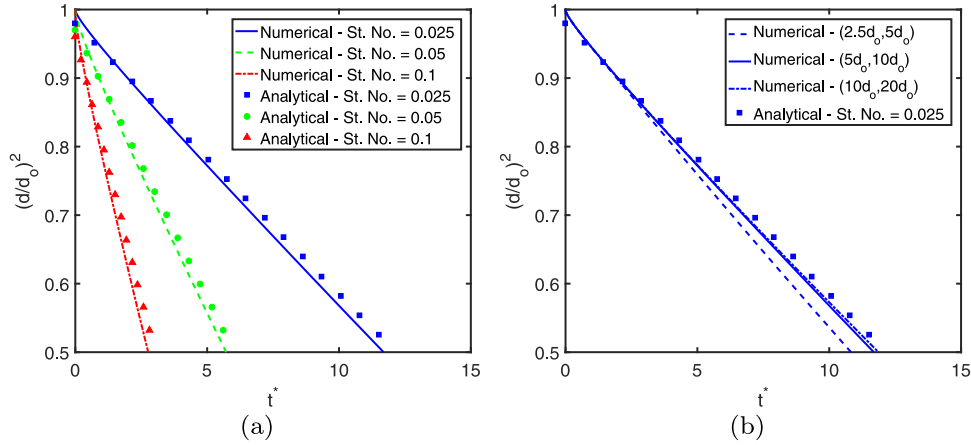


**Fig. 7.** (a) Comparison of the analytical and numerical results for the normalized  $d^2$  plotted against the non-dimensional time for  $St = 0.025, 0.05$  and  $0.1$ . The computational domain is  $5d_0$  and  $10d_0$  in the radial and axial directions, respectively. Grid:  $256 \times 512$ . (b) The effects of the computational domain size on the numerical results for  $St = 0.025$ . The results are obtained for the domain sizes of  $(2.5d_0, 5d_0)$ ,  $(5d_0, 10d_0)$  and  $(10d_0, 20d_0)$  in  $(r, z)$  coordinate directions, respectively. The respective grid resolutions are:  $128 \times 256$ ,  $256 \times 512$  and  $512 \times 1024$ . ( $\gamma = 5$  and  $\zeta = 10$ ).

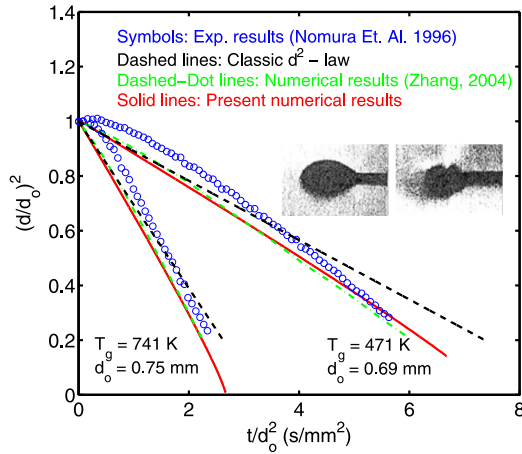


**Fig. 8.** The square of the normalized droplet diameter against the scaled time for an evaporating *n*-heptane droplet. The present results are compared with the experimental data and the previous numerical results as well as with the classical  $d^2$ -law for two different initial gas phase temperatures and diameters. Insets show two snapshots from the experimental results of Nomura et al. [40] during the evaporation process. ( $\gamma = 100$  and  $\zeta = 10$ ).

as 300 K whereas initial gas phase temperature  $T_g$  is applied as the Dirichlet temperature boundary condition at the walls. The density and viscosity ratios are set as 100 and 10, respectively. Higher density ratio is also tested but no significant effect on the results is observed. The gas phase thermophysical properties are evaluated at the boiling temperature and are assumed to stay constant during the whole simulation as suggested by Miller et al. [42]. As seen in Fig. 8, the present numerical results are in good agreement with the numerical results of Zhang [43]. Also, the present results overall follow the trends of the experimental results, however, some deviations are observed especially in the initial stages of the evaporation process. The possible reasons are highlighted below.

1. As shown in the inset of Fig. 8, the snapshots of the evaporating droplet taken during the experiments [40] reveal that the droplet is far from a spherical shape in the experiment whereas it remains nearly spherical throughout the numerical simulations.
2. In the experiments, the droplet is generated at the tip of a silica fiber whereas no such effects are considered in the numerical simulations. In the literature, several experimental and numer-

ical studies are available to show the influence of supporting fiber on the droplet heat and mass transfer [32,74,75].

3. In the experiments, the droplet is introduced into the hot environment by translating it through some distance which may have introduced some convective currents. This is probably the reason for the flat portion seen at the start of the experimental results, as also argued by Zhang [43]. Also, the liquid needs to reach its saturation temperature which may have produced initial plateau on the  $d^2$  curve.
4. Another possible reason may be the fact that in the numerical study, the gas phase thermo-physical properties are evaluated at the boiling temperature and are assumed to stay constant during the whole simulation, as suggested by Miller et al. [42]. However, the numerical experiments suggest that this assumption produce negligible changes, as also confirmed by the validation results described in the later sections.

The order of accuracy of our numerical algorithm has been demonstrated in our previous study to be around 1.5 for a static evaporating droplet and unity for the extremely deformed moving evaporation droplets [1].

#### 4.3. Combustion of an evaporating droplet

Finally, the combustion of an evaporating droplet is simulated by incorporating the CHEMKIN package into our phase change solver as explained in Section 3.3. Accurate incorporation of the CHEMKIN package is first verified using a standard test case of the hydrogen-air combustion under the constant pressure conditions [57]. The results reported in the manual [57] for the species mole fractions and temperature are exactly reproduced using the current solver. This verifies the accurate incorporation of the chemical kinetics solver (CHEMKIN) when triggered from our main code. To test the full functionality of the code, i.e., the correct coupling of the multiphase phase change and combustion solvers, comprehensive test cases are simulated that involve the combustion of an evaporating droplet in quiescent hot air environment using a single-step and a detailed chemistry models.

##### 4.3.1. Single step chemistry

The evaporation and combustion of a *n*-heptane droplet is studied and the numerical results are compared with the previous numerical results [44,58] and the experimental data [76–78]. We made some simplifying assumptions for this analysis: The Marangoni, Soret and Dufour effects are neglected, radiative heat

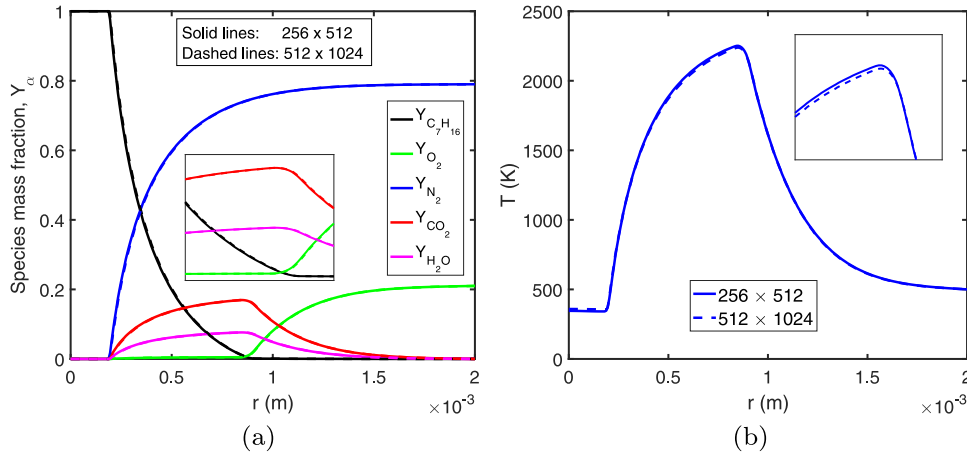


**Fig. 9.** Grid convergence study: The profiles of (a) the species mass fractions and (b) the temperature plotted along the horizontal centerline computed using  $256 \times 512$  (coarse) and  $512 \times 1024$  (fine) grid resolutions at  $t/d_o^2 = 0.09375$  s/mm<sup>2</sup>. The insets show the magnified views around the sharp gradients. The small difference between the results obtained using the coarse and the fine grid resolutions indicates the grid convergence. (For interpretation of the references to color in this figure legend, the reader is referred to the web version of this article.)

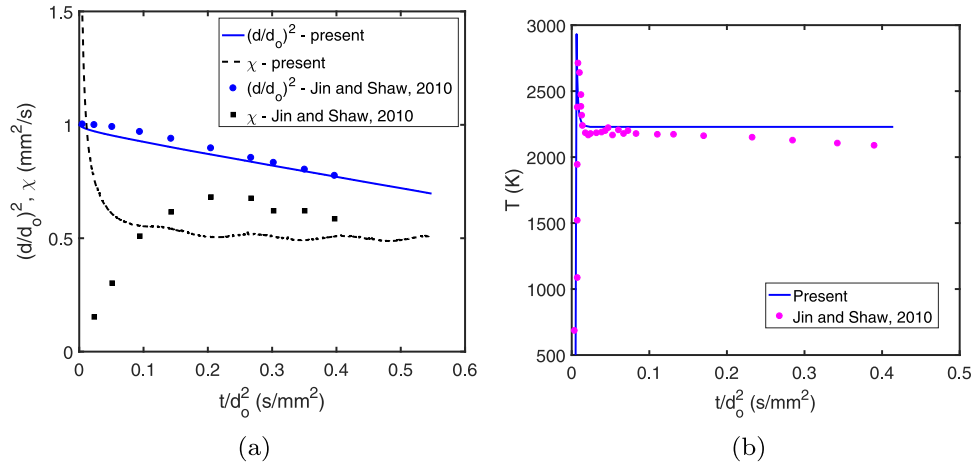


**Fig. 10.** (a) Comparison of the present and the previous numerical results for the variation of the normalized  $d^2$  and the fuel gasification rate  $\chi$  for an evaporating and burning *n*-heptane droplet with the scaled time  $t/d_o^2$ . The gasification rate  $\chi$  approximately attains a steady state value at  $t/d_o^2 = 0.15$  s/mm<sup>2</sup> for the present case. (b) The peak values of the gas phase temperatures plotted against  $t/d_o^2$  and compared with the previous numerical results. The present results approach a steady state value whereas results of Jin and Shaw [58] continue to decrease. The initial droplet diameter is  $d_o = 0.4$  mm. Grid:  $256 \times 512$ .

transfer is not taken into account and a local thermodynamics equilibrium is assumed to be attained at the droplet interface. We assume a single-step chemistry with constant thermodynamics properties and unity Lewis number for all the species. In addition, an ideal gas behavior is assumed in the gas phase. The global single-step chemical mechanism for *n*-heptane can be written as



A section of *n*-heptane droplet is actually simulated by exploiting the axisymmetry condition at the centerline as schematically shown in Fig. 1. The initial diameter of the droplet is  $d_o = 0.4$  mm and is placed at the centerline with the center point coordinates as  $(r_o, z_o) = (0, 2)$  mm. The computational domain is  $5d_o$  and  $10d_o$  in the radial and the axial directions, respectively, and is resolved using  $256 \times 512$  uniform grid cells. The droplet temperature is initialized as the boiling point of the *n*-heptane, i.e.,  $T_o = T_b = 371.6$  K. The initial fuel vapor mass fraction at the interface is 1 whereas all other species mass fractions are initialized as 0; the same values are applied as the species mass fraction boundary conditions at the interface throughout the simulations. The temperature in the ambient air is initialized uniformly at 500 K. The gas domain is assumed to be pure air composed of 79%  $N_2$  and 21%  $O_2$  by volume. The evaporation of *n*-heptane droplet produces

fuel vapors around the droplet which react with the oxidizer in the air to produce the combustion products. Eq. (6) is solved for all the species in the gas domain at each time step to obtain an updated species field. At the domain boundaries, the temperature and species boundary conditions are 500 K and pure air, respectively. It is observed that the fuel-air mixture does not automatically ignite unless the ignition energy is supplied by artificially increasing the temperature locally using an external heat source. In the present study, the temperature is increased to 1800 K in the gas domain around the droplet for 50 time steps subjected to the conditions:  $Y_{C_7H_{16}} > 0.01$  and  $Y_{O_2} > 0.01$ . Once the fuel is ignited the combustion proceeds in a smooth fashion.

First a grid convergence study is performed; results are presented for species mass fractions and temperature for two grid resolutions:  $256 \times 512$  and  $512 \times 1024$ , as shown in Fig. 9. Species mass fraction profiles almost overlap for the two grids used whereas the temperature profile shows a small difference near the peak. Hence the  $256 \times 512$  grid resolution is used for the rest of the study unless specified otherwise. Results are then presented for the variation of normalized squared-diameter  $(d/d_o)^2$  and the fuel gasification rate  $\chi$  with the scaled time of  $t/d_o^2$ , as shown in Fig. 10(a). The fuel gasification rate is defined as  $\chi = -d(d^2)/dt$ , where  $d$  is the instantaneous droplet diameter. As seen

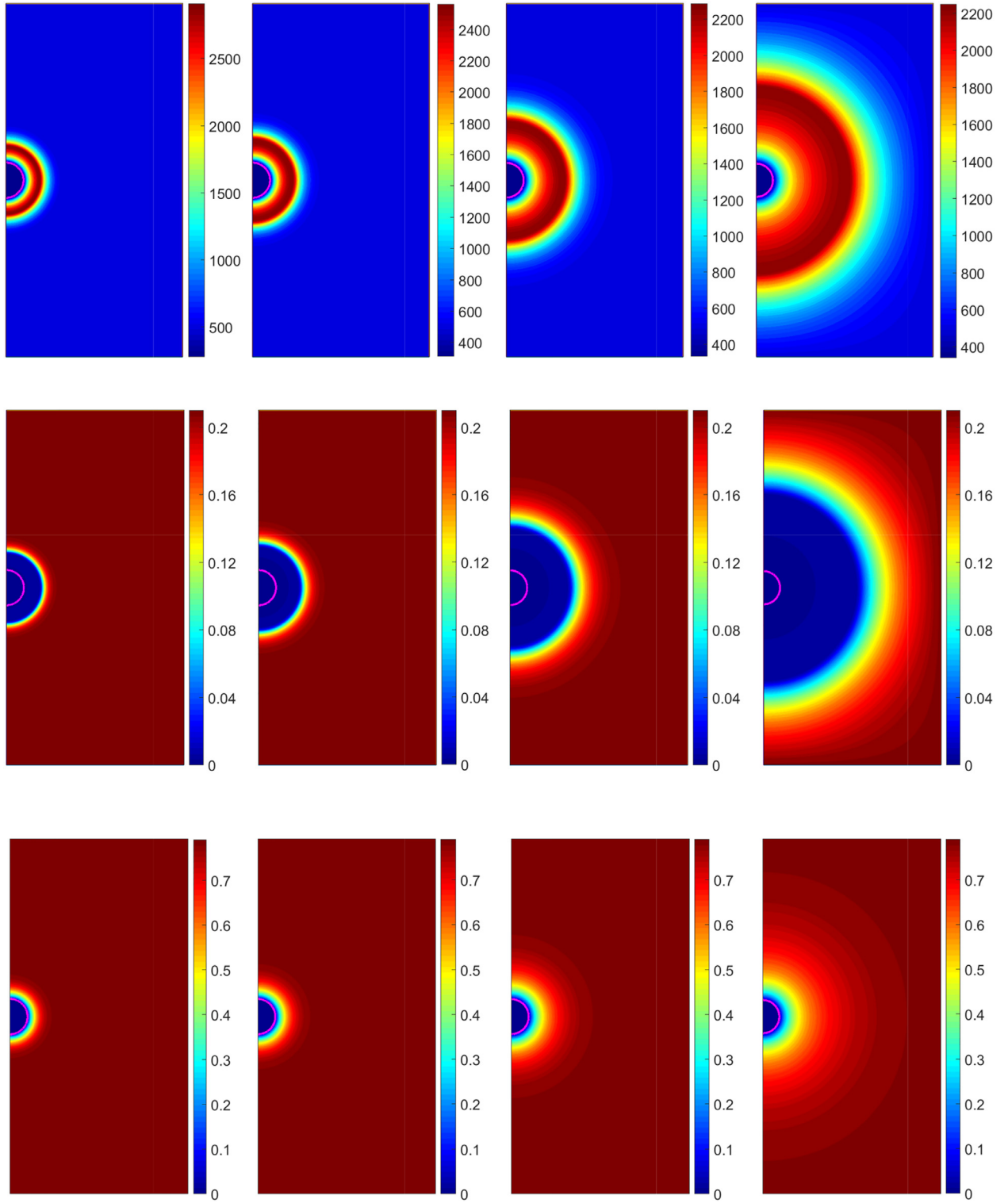


**Fig. 11.** The contour plots of temperature (top row), oxygen mass fraction (middle row) and nitrogen mass fraction (bottom row) showing their evolution in time for an evaporating and burning *n*-heptane droplet at (from left to right in each row)  $t/d_0^2 = 0.00375, 0.0084, 0.0343$  and  $0.1875$  s/mm<sup>2</sup>. The initial droplet diameter is  $d_0 = 0.4$  mm. Grid:  $256 \times 512$ . (For interpretation of the references to color in this figure legend, the reader is referred to the web version of this article.)

in Fig. 10(a), the present numerical results compare well and generally follow the trends of the previous numerical study [58]. The difference observed, which is more significant at the initial stages, is attributed mainly to the differences in the computational and operating parameters, e.g., the domain size, thermophysical proper-

ties, the ignition heat source strength and its duration, etc. During the course of the simulation there is an initial vaporization phase at the beginning when fuel vaporizes but there is no combustion. Once sufficient amount of heat is supplied, the ignition starts and a partially premixed flame first develops near the droplet which then

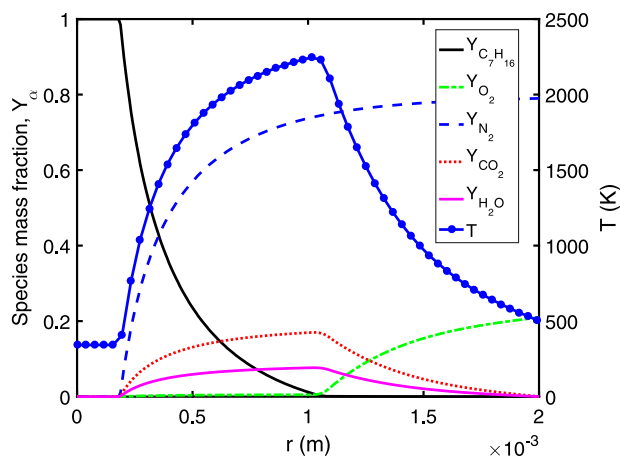


**Fig. 12.** The profiles of temperature and species mass fractions along the horizontal centerline ( $z = 5d_o$ ) of the domain at time  $t/d_o^2 = 0.1875 \text{ s/mm}^2$ . The peak temperature indicates the location of the flame front where the species mass fraction profiles also show a sharp gradient. The initial droplet diameter is  $d_o = 0.4 \text{ mm}$ . Grid:  $256 \times 512$ . (For interpretation of the references to color in this figure legend, the reader is referred to the web version of this article.)

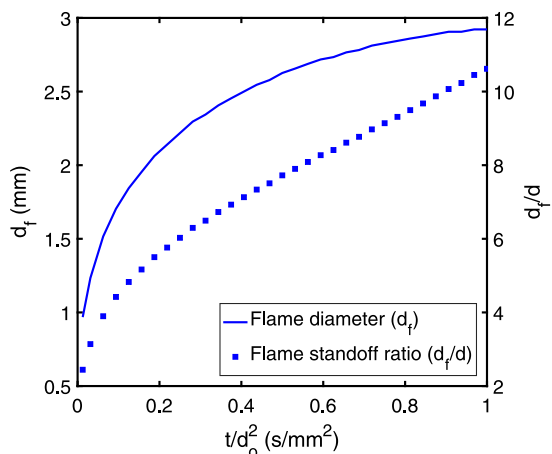


**Fig. 13.** The flame diameter ( $d_f$ ) and the standoff ratio ( $d_f/d$ ) plotted against  $t/d_o^2$  for a burning *n*-heptane droplet ( $d_o = 0.4 \text{ mm}$ ). The flame diameter approaches to a steady state value provided that the computational domain is sufficiently large. However, the standoff ratio is expected to increase till the whole droplet is burnt out. The domain size for this case is  $10d_o$  and  $20d_o$  in the radial and the axial directions, respectively. Grid:  $512 \times 1024$ .

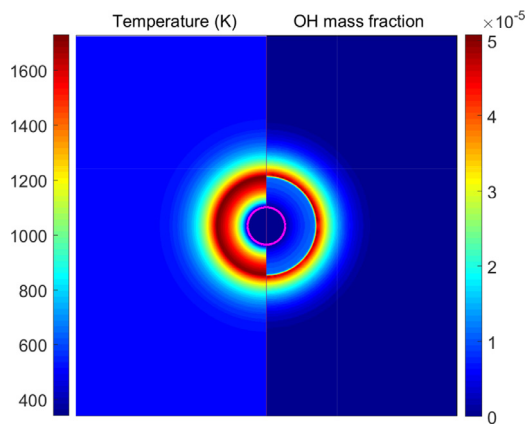


**Fig. 14.** The constant contour plots of temperature (left portion) and OH mass fraction (right portion) for a burning *n*-heptane droplet at  $t = 5.5 \text{ ms}$  using the reduced chemical kinetic mechanism of Maroteaux and Noel [79]. The gas phase temperature is  $T_g = 500 \text{ K}$  and pressure  $p = 10 \text{ atm}$ . The domain size is  $5d_o$  and  $10d_o$  in the radial and the axial directions, respectively. ( $d_o = 0.4 \text{ mm}$ ; Grid:  $256 \times 512$ ). (For interpretation of the references to color in this figure legend, the reader is referred to the web version of this article.)

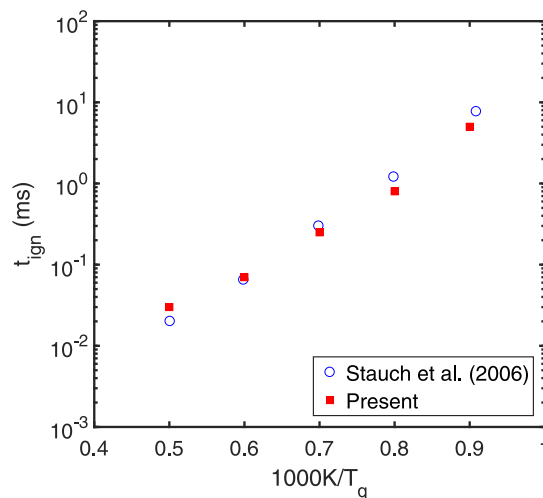


**Fig. 15.** The detailed chemistry calculations of the ignition delay time  $t_{\text{ign}}$  for the *n*-heptane droplet. The present results are plotted together with the numerical results of Stauch et al. [45] for various gas phase temperatures ( $T_g$ ) at the fixed pressure of  $p = 7 \text{ atm}$ . The computational domain:  $2.5d_o \times 5d_o$ ;  $d_o = 0.4 \text{ mm}$ ; Grid:  $128 \times 256$ .

transforms into a diffusion flame. The close proximity of the flame induces excessive droplet vaporization, pushing the flame outwards [44]. This transient phase with high vaporization/gasification rates results in a fast reduction in the droplet area, i.e.,  $d^2$ . These trends are clearly visible for both the results of  $(d/d_o)^2$  and  $\chi$  during the early stages of combustion as shown in Fig. 10(a). Similar trends are also reported by Cho and Dryer [44] during the unsteady burning phase. In contrast, the numerical results of Jin and Shaw [58] show a more extended ignition delay time and low gasification rate at the initial stages. This is mainly due to the two reasons. First, the heat source for igniting the fuel droplet is applied after a longer initial vaporization phase as compared to the present study due to which the gasification rate is much lower during that initial phase; that phase is not visible in the results of the present study. Second, the strength of the ignition heat source is weak as compared to the present study therefore the peak gasification rates attained are lower when compared to the present results. The peak temperatures produced in the gas domain as a result of chemical reaction are plotted and compared with the previous numerical results [58] in Fig. 10(b). This figure shows that a temperature spike is produced as the reaction starts which gradually smooths out to a steady state value. The similar observation is also reported by Cho and Dryer in their numerical study about *n*-heptane droplet burning [44]. Fig. 11 shows the temperature and species mass fraction contour plots for oxygen and nitrogen at four different instants during the droplet burning showing their evolution in time during the course of combustion. A flame is produced which diffuses outwards maintaining the spherical symmetry. Profiles of the species mass fractions and temperature at  $z = 5d_o$  are plotted in Fig. 12. The peak temperature marks the location of the flame front: to the left of this point there is no oxidizer and to the right there is no fuel. All the fuel transported to the flame front is burnt to produce the combustion products. There is an equilibrium between the fuel gasification and consumption, termed as the steady state condition; the flame temperature being constant during that condition.

The initial flame diameter  $d_f$  obtained in the current study is approximately  $1 \text{ mm}$  which continuously increases before reaching a steady state value. This trend is shown in Fig. 13 along with the flame standoff ratio ( $d_f/d$ ). For this particular test case a bigger computational domain is used so that the flame size can reach a steady state value. The computational domain is  $10d_o$  and  $20d_o$  in

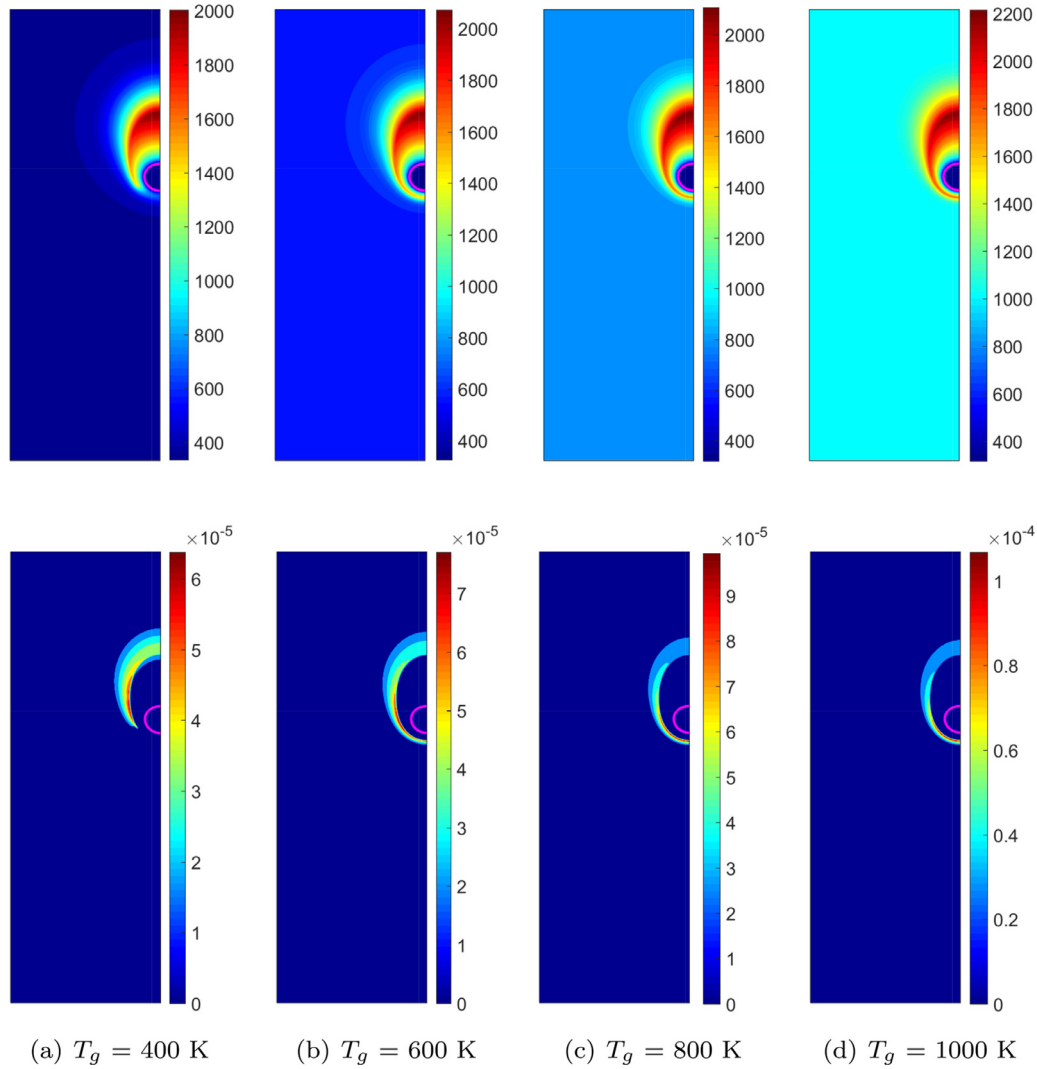


**Fig. 16.** Contour plots of temperature (top row) and OH mass fraction (bottom row) for a burning *n*-heptane droplet at  $t = 3.0$  ms using the reduced chemical kinetic mechanism comprising of 25-species and 26-reactions [79]. The domain size is  $5d_o$  in radial and  $15d_o$  in axial directions where the initial diameter  $d_o = 0.4$  mm and  $p = 10$  atm. Grid:  $256 \times 768$ . The gas phase temperature  $T_g$  is varied to analyze the effects on the flame extinction/blow-off. (For interpretation of the references to color in this figure legend, the reader is referred to the web version of this article.)

the radial and the axial directions, respectively, and is resolved using  $512 \times 1024$  grid cells. It is observed that the ignition starts with a standoff value of 2.5; this is consistent with the previous numerical studies [44,58]. The standoff value follows the trend of flame diameter but continues to increase linearly as expected, and more quickly towards the end of droplet life time, because the droplet diameter  $d$  is continuously decreasing.

#### 4.3.2. Detailed chemistry calculations

Finally, simulations are performed for the evaporation and combustion of a *n*-heptane droplet using a detailed chemical kinetic model. For this purpose, the reduced chemical kinetic mechanism of Maroteaux and Noel [79] is incorporated into the numerical algorithm to rigorously test the functionality of our solver. The reduced mechanism includes 25 species and 26 reactions.

We first consider the evaporation and burning of the *n*-heptane droplet case described in Section 4.3.1 but the simulations are now performed using the reduced chemical kinetic mechanism of Maroteaux and Noel [79]. The constant contours of the temperature and the OH mass fraction are plotted side by side sharing the common centerline as shown in Fig. 14. The contours of the maximum temperature and the OH mass fraction coincide to mark the location of the propagating flame front, which is quite expected as

both quantities are widely used to determine the location of the flame front in the combustion literature [51]. To verify our results quantitatively, a test case is simulated to determine the ignition delay times ( $t_{ign}$ ) during the autoignition of a *n*-heptane droplet under isobaric conditions for various values of the gas phase temperature  $T_g$ . In contrary to our previous simulations, there is no localized artificial heating of the gas domain near the droplet in this particular test case since we are focusing on the autoignition. Comparison is made with the numerical results of Stauch et al. [45] who also studied a similar case to analyze the effect of gas phase temperature on the ignition delay times. The results compare very well as shown in Fig. 15 despite the fact that there are some differences in the physical and computational settings for the two compared cases. Also, Stauch et al. [45] used a more detailed chemical mechanism as compared to the present study. It is observed that the ignition delay time is a strong function of gas phase temperature and decreases as the gas phase temperature is increased. The computational cost analysis is also performed for the case with  $T_g = 2000$  K. It is found that approximately 85% of the total computational time is utilized by the CHEMKIN solver.

Next, the method is applied to simulate the case of a burning *n*-heptane droplet moving in a gaseous ambient environment



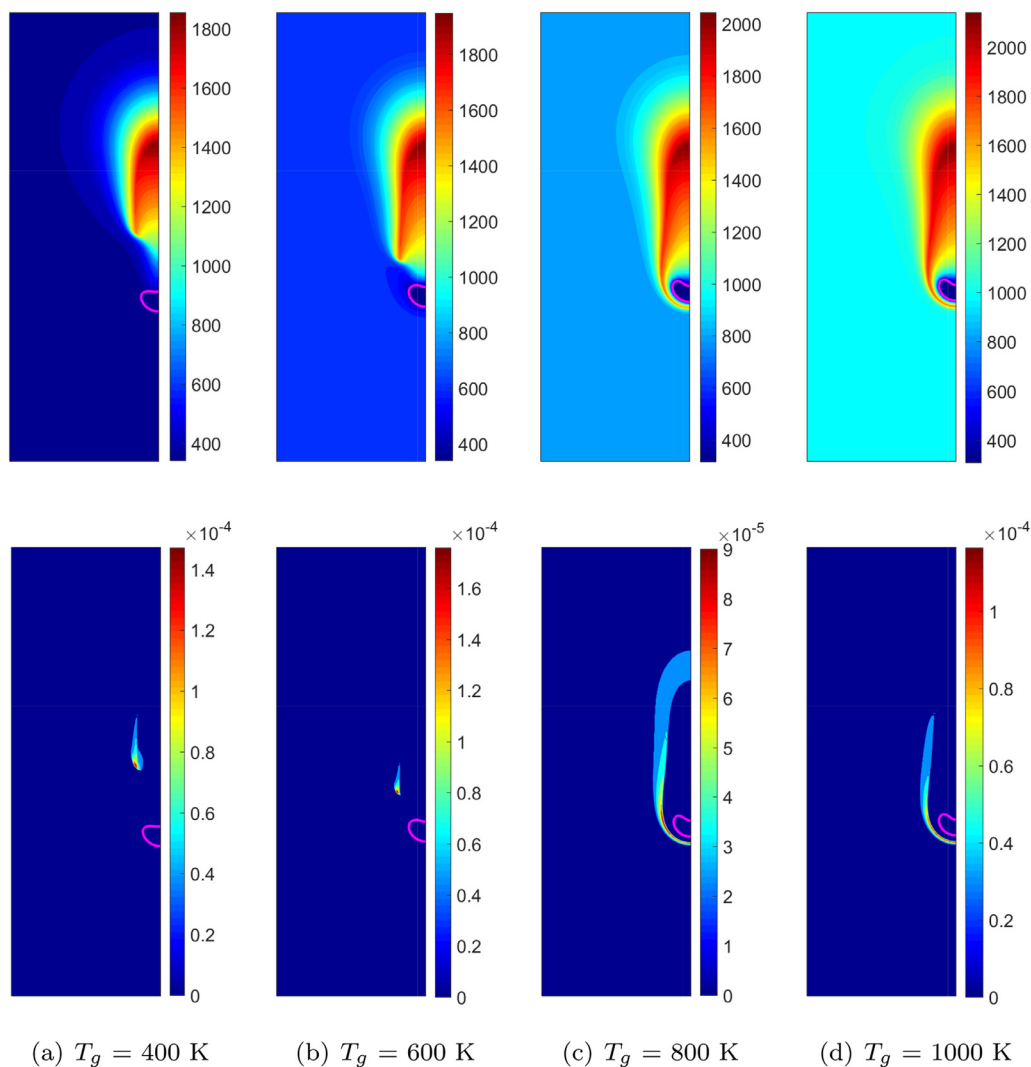


**Fig. 17.** Contour plots of temperature (top row) and OH mass fraction (bottom row) for a burning *n*-heptane droplet at  $t = 5.5$  ms using reduced chemical kinetic mechanism comprising of 25-species and 26-reactions [79]. The domain size is  $5d_o$  in radial and  $15d_o$  in axial directions where initial diameter  $d_o = 0.4$  mm and  $p = 10$  atm. Grid:  $256 \times 768$ . The gas phase temperature  $T_g$  is varied to analyze the effects on the flame extinction/blow-off. (For interpretation of the references to color in this figure legend, the reader is referred to the web version of this article.)

under the action of gravity with the Eotvos number  $Eu = 62.08$ , the Ohnesorge number for droplet  $Oh_d = 0.14$  and the Ohnesorge number for ambient fluid  $Oh_o = 0.082$ . The density and viscosity of the ambient fluid (air) are increased in solving the flow equations mainly to enhance the numerical stability, i.e., the density and the viscosity ratios are set to  $\gamma = 33.33$   $\zeta = 10$ , respectively, in the hydrodynamics calculations. We note that a further increase in the density and viscosity ratios does not affect the computational results significantly. The actual physical material properties are used in the thermo-chemical calculations. A droplet of initial diameter  $d_o = 0.4$  mm is placed at the centerline with the center point coordinates  $(r_o, z_o) = (0, 11.25d_o)$ . The domain size is  $5d_o$  and  $15d_o$  in the radial and axial directions, respectively; and is resolved using  $256 \times 768$  grid points. Pressure in the domain is set as 10 atm and gas phase temperature  $T_g$  is varied from 400 K to 1000 K for different test cases. Artificial heat source is applied to ignite the fuel as explained in Section 4.3.1. The same section describes the implementation of temperature and species mass fraction boundary conditions. Fig. 16 shows the contour plots of temperature and OH mass fraction at  $t = 3.0$  ms. It is observed from the plots that the gas phase temperature controls the extinction/blow-off of the flame. For low ambient temperature, i.e.,  $T_g = 400$  K, the flame ex-

tingtion has started at the front section of the droplet as shown by the contours of the OH mass fraction. This is also supported by the low temperature region produced at the front face of the falling droplet. For the rest of the cases, the flame is intact as shown by the OH mass fraction which marks the location of flame front; the temperature contours also surround the droplet supporting the existence of flame.

The temperature and the OH mass fraction contours are then plotted at time  $t = 5.5$  ms to observe the flame characteristics of a moving droplet at a later stage for different values of  $T_g$  as shown in Fig. 17. The flame blow-off occurs for the cases with  $T_g = 400$  K and 600 K, since the ambient temperature is not high enough to keep the flame burning once it is artificially ignited initially. However, for large values of  $T_g$ , sufficient energy is continuously available to sustain the chemical reaction and hence flame exists resulting high temperatures that envelope the droplet. It is interesting to note that a moving droplet that is burning as well deforms more as compared to the one that just evaporates as shown in Fig. 17. The present results also verify the applicability of our numerical method to significantly deformed burning droplets in the engine-like environment with good degree of accuracy.

## 5. Conclusions

A finite-difference/front-tracking method is developed to simulate the evaporation and combustion of a fuel droplet in a gaseous ambient environment. A one-field formulation of the governing equations is solved on a fixed, uniform and staggered grid. The interface is represented by a Lagrangian grid consisting of connected marker points that are tracked explicitly. The Navier–Stokes equations are solved using a projection method satisfying the modified continuity equation; that modification arises due to the phase change at the interface. A splitting scheme is employed to decouple the chemical kinetics and the CFD components of the energy and species conservation equations. The chemistry part is solved using the CHEMKIN package in combination with the stiff ODE solver of VODE. The solution for the temperature and species mass fraction is advanced in time using an explicit Euler method. Peskin's interpolation function is used to communicate between the fixed grid and the interface.

First, the base multiphase solver is successfully validated for the gravity driven falling droplets studied computationally by Han and Tryggvason [71]. The temperature gradient based phase change solver is then incorporated into the multiphase solver and results are compared with the analytical solutions, the experimental data and the previous numerical studies. The  $d^2$ -law is demonstrated for a static evaporating droplet case for various Stefan numbers. The  $n$ -heptane droplet evaporation is then simulated and results are compared with the experimental data as well as the previous numerical results with good degree of accuracy. The evaporated fuel vapors then undergo chemical reaction with the ambient air to produce the reaction products. We successfully used a simple single-step as well as a detailed chemical kinetic mechanism for simulations of the  $n$ -heptane fuel droplet combustion. The gasification rate, normalized  $d^2$  and peak temperatures compare well with the previous numerical results; the discrepancies arise mainly due to slight differences in the computational domain setup, the operating parameters and the chemical kinetic mechanisms. The constant contours and the line plots of the temperature and the species mass fractions qualitatively confirm the accuracy of our results. The initial flame diameter and the flame standoff ratio also compare well with the previous studies. The numerical results of the ignition time delay for a  $n$ -heptane droplet combustion for different ambient temperatures show an excellent agreement with the previous numerical results of Stauch et al. [45]. The method is finally applied to a  $n$ -heptane droplet moving due to gravity in various ambient temperature conditions yielding interesting results about flame blow-off. Ambient temperature is found to be an influencing parameter in this regard. The numerical method is overall second order accurate in space but it is a known fact that the spatial accuracy reduces to first order for the global mass conservation mainly due to the smoothing of discontinuous fields such as evaporation mass source in the vicinity of the interface. The present numerical results can be compared with the experiments only in a qualitative sense because a real burning droplet experiences various degrees of motion relative to the gas and contains a significant amount of soot in the flame envelope which is not considered here [44]. The more detailed chemistry and variable transport and thermodynamic properties are expected to further enhance the quality of our results.

The present work lays the foundation for direct numerical simulations of spray combustion in actual compression-ignition engine conditions. Towards this ultimate goal, the future work includes extension of the present numerical method to full 3D geometries as Muradoglu and Tryggvason [70] did for the simulation of soluble surfactant. The computational cost is expected to approximately scale with the 3rd dimension.

## Acknowledgments

The first author is supported by The Higher Education Commission of Pakistan under HRDI-UESTP program. Computations are performed at HPC facility of the Koc University.

## References

- [1] Irfan M, Muradoglu M. A front tracking method for direct numerical simulation of evaporation process in a multiphase system. *J Comput Phys* 2017;337:132–53. doi:10.1016/j.jcp.2017.02.036. <http://www.sciencedirect.com/science/article/pii/S0021999117301304>
- [2] Harlow FH, Welch JE. Numerical calculation of time?Dependent viscous incompressible flow of fluid with free surface. *Phys Fluids* 1965;8(12):2182–9. doi:10.1063/1.1761178.
- [3] Hirt C, Nichols B. Volume of fluid (VOF) method for the dynamics of free boundaries. *J Comput Phys* 1981;39(1):201–25. doi:10.1016/0021-9991(81)90145-5.
- [4] Osher S, Sethian JA. Fronts propagating with curvature-dependent speed: algorithms based on hamilton-jacobi formulations. *J Comput Phys* 1988;79(1):12–49. doi:10.1016/0021-9991(88)90002-2.
- [5] Sussman M, Smereka P, Osher S. A level set approach for computing solutions to incompressible two-phase flow. *J Comput Phys* 1994;114(1):146–59. doi:10.1006/jcph.1994.1155.
- [6] Jacqmin D. Calculation of two-phase Navier–Stokes flows using phase-field modeling. *J Comput Phys* 1999;155(1):96–127. doi:10.1006/jcph.1999.6332.
- [7] Anderson DM, McFadden GB, Wheeler AA. Diffuse-interface methods in fluid mechanics. *Annu Rev Fluid Mech* 1998;30(1):139–65. doi:10.1146/annurev.fluid.30.1.139.
- [8] Swift MR, Orlandini E, Osborn WR, Yeomans JM. Lattice Boltzmann simulations of liquid-gas and binary fluid systems. *Phys Rev E* 1996;54:5041–52. doi:10.1103/PhysRevE.54.5041. <https://link.aps.org/doi/10.1103/PhysRevE.54.5041>
- [9] Ryskin G, Leal LG. Numerical solution of free-boundary problems in fluid mechanics. part 1. the finite-difference technique. *J Fluid Mech* 1984;148:1–17. doi:10.1017/S00222112084002214.
- [10] Glimm J. Nonlinear and stochastic phenomena: the grand challenge for partial differential equations. *SIAM Rev* 1991;33(4):626–43. doi:10.1137/1033137.
- [11] Unverdi SO, Tryggvason G. A front-tracking method for viscous, incompressible, multi-fluid flows. *J Comput Phys* 1992;100(1):25–37. doi:10.1016/0021-9991(92)90307-K.
- [12] Tryggvason G, Bunner B, Esmaeili A, Juric D, Al-Rawahi N, Tauber W, Han J, Nas S, Jan YJ. A front-tracking method for the computations of multiphase flow. *J Comput Phys* 2001;169(2):708–59. doi:10.1006/jcph.2001.6726.
- [13] Juric D, Tryggvason G. Computations of boiling flows. *Int J Multiph Flow* 1998;24(3):387–410. doi:10.1016/S0301-9322(97)00050-5.
- [14] Esmaeili A, Tryggvason G. Computations of film boiling. part i: numerical method. *Int J Heat Mass Transf* 2004a;47(25):5451–61. doi:10.1016/j.ijheatmasstransfer.2004.07.027.
- [15] Esmaeili A, Tryggvason G. Computations of explosive boiling in microgravity. *J Sci Comput* 2003;19(1):163–82. doi:10.1023/A:1025347823928.
- [16] Esmaeili A, Tryggvason G. A front tracking method for computations of boiling in complex geometries. *Int J Multiph Flow* 2004b;30(7):1037–50. doi:10.1016/j.ijmultiphaseflow.2004.04.008. A Collection of Papers in Honor of Professor G. Yadigaroglu on the Occasion of his 65th Birthday. <http://www.sciencedirect.com/science/article/pii/S0301932204000576>
- [17] Esmaeili A, Tryggvason G. Computations of film boiling. part ii: multi-mode film boiling. *Int J Heat Mass Transf* 2004c;47(25):5463–76. doi:10.1016/j.ijheatmasstransfer.2004.07.028. <http://www.sciencedirect.com/science/article/pii/S0017931004002959>
- [18] Al-Rawahi N, Tryggvason G. Numerical simulation of dendritic solidification with convection: two-dimensional geometry. *J Comput Phys* 2002;180(2):471–96. doi:10.1006/jcph.2002.7092.
- [19] Al-Rawahi N, Tryggvason G. Numerical simulation of dendritic solidification with convection: three-dimensional flow. *J Comput Phys* 2004;194(2):677–96. doi:10.1016/j.jcp.2003.09.020. <http://www.sciencedirect.com/science/article/pii/S0021999103005011>
- [20] Juric D, Tryggvason G. A front-tracking method for dendritic solidification. *J Comput Phys* 1996;123(1):127–48. doi:10.1006/jcph.1996.0011. <http://www.sciencedirect.com/science/article/pii/S002199919690011X>
- [21] Vu TV, Tryggvason G, Homma S, Wells JC. Numerical investigations of drop solidification on a cold plate in the presence of volume change. *Int J Multiph Flow* 2015;76:73–85. doi:10.1016/j.ijmultiphaseflow.2015.07.005. <http://www.sciencedirect.com/science/article/pii/S0301932215001585>
- [22] Qian J, Tryggvason G, Law C. A front tracking method for the motion of premixed flames. *J Comput Phys* 1998;144(1):52–69. doi:10.1006/jcph.1998.5991.
- [23] Koynov A, Khinast JG, Tryggvason G. Mass transfer and chemical reactions in bubble swarms with dynamic interfaces. *AIChE J* 2005;51(10):2786–800. doi:10.1002/aic.10529.
- [24] Aboulhasanzadeh B, Thomas S, Taeibi-Rahni M, Tryggvason G. Multiscale computations of mass transfer from buoyant bubbles. *Chem Eng Sci* 2012;75:456–67. doi:10.1016/j.ces.2012.04.005.
- [25] Godsave G. Studies of the combustion of drops in a fuel spray?the burning of single drops of fuel. *Symp Int Combust* 1953;4(1):818–30.

- doi:10.1016/S0082-0784(53)80107-4. <http://www.sciencedirect.com/science/article/pii/S0082078453801074>
- [26] Spalding D. The combustion of liquid fuels. *Symp Int Combust* 1953;4(1):847–64. doi:10.1016/S0082-0784(53)80110-4. <http://www.sciencedirect.com/science/article/pii/S0082078453801104>
- [27] Faeth G. Current status of droplet and liquid combustion. *Prog Energy Combust Sci* 1977;3(4):191–224. doi:10.1016/0360-1285(77)90012-0. <http://www.sciencedirect.com/science/article/pii/S0360128577900120>
- [28] Law C, Chung S, Srinivasan N. Gas-phase quasi-steadiness and fuel vapor accumulation effects in droplet burning. *Combust Flame* 1980;38:173–98. doi:10.1016/0010-2180(80)90049-8. <http://www.sciencedirect.com/science/article/pii/S0010218080900498>
- [29] Law C. Recent advances in droplet vaporization and combustion. *Prog Energy Combust Sci* 1982;8(3):171–201. doi:10.1016/0360-1285(82)90011-9. <http://www.sciencedirect.com/science/article/pii/S0360128582900119>
- [30] Sirignano WA. Fuel droplet vaporization and spray combustion theory. *Prog Energy Combust Sci* 1983;9(4):291–322. doi:10.1016/0360-1285(83)90011-4. <http://www.sciencedirect.com/science/article/pii/S0360128583900114>
- [31] Lefebvre AH. Atomization and sprays. New York: Hemisphere Publishing Corporation; 1989.
- [32] Toker G, Stricker J. Holographic study of suspended vaporizing volatile liquid droplets in still air. *Int J Heat Mass Transfer* 1996;39(16):3475–82. doi:10.1016/0017-9310(96)00018-X. <http://www.sciencedirect.com/science/article/pii/S001793109600018X>
- [33] Sazhin S, Abdelghaffar W, Sazhina E, Heikal M. Models for droplet transient heating: effects on droplet evaporation, ignition, and break-up. *Int J Therm Sci* 2005;44(7):610–22. doi:10.1016/j.ijthermalsci.2005.02.004. <http://www.sciencedirect.com/science/article/pii/S1290072905000517>
- [34] Abramzon B, Sirignano W. Droplet vaporization model for spray combustion calculations. *Int J Heat Mass Transfer* 1989;32(9):1605–18. doi:10.1016/0017-9310(89)90043-4. <http://www.sciencedirect.com/science/article/pii/S0017931089900434>
- [35] Sazhin SS. Advanced models of fuel droplet heating and evaporation. *Prog Energy Combust Sci* 2006;32(2):162–214. doi:10.1016/j.pecs.2005.11.001. <http://www.sciencedirect.com/science/article/pii/S0360128505000535>
- [36] Sirignano WA. Fluid dynamics and transport of droplets and sprays. 2. Cambridge University Press; 2010. doi:10.1017/CBO9780511806728.003.
- [37] Downing CG. The evaporation of drops of pure liquids at elevated temperatures: rates of evaporation and wet-bulb temperatures. *AIChE J* 1966;12(4):760–6. doi:10.1002/aic.690120424. <https://doi.org/10.1002/aic.690120424>
- [38] Yuen MC, Chen LW. On drag of evaporating liquid droplets. *Comb Sci Tech* 1976;14(4–6):147–54. doi:10.1080/00102207608547524. <https://doi.org/10.1080/00102207608547524>
- [39] Wong SC, Lin AC. Internal temperature distributions of droplets vaporizing in high-temperature convective flows. *J Fluid Mech* 1992;237:671–87. doi:10.1017/S0022112092003574.
- [40] Nomura H, Ujiie Y, Rath HJ, Sato J, Kono M. Experimental study on high-pressure droplet evaporation using microgravity conditions. *Proc Combust Inst* 1996;26(1):1267–73. doi:10.1016/S0082-0784(96)80344-4. <http://www.sciencedirect.com/science/article/pii/S0082078496803444>
- [41] Dietrich DL, Struk PM, Ikegami M, Xu G. Single droplet combustion of decane in microgravity: experiments and numerical modelling. *Combust Theory Model* 2005;9(4):569–85. doi:10.1080/13647830500256039. <https://doi.org/10.1080/13647830500256039>
- [42] Miller R, Harstad K, Bellan J. Evaluation of equilibrium and non-equilibrium evaporation models for many-droplet gas-liquid flow simulations. *Int J Multiphase Flow* 1998;24(6):1025–55. doi:10.1016/S0301-9322(98)00028-7. <http://www.sciencedirect.com/science/article/pii/S0301932298000287>
- [43] Zhang H. Numerical research on a vaporizing fuel droplet in a forced convective environment. *Int J Multiphase Flow* 2004;30(2):181–98. doi:10.1016/j.ijmultiphaseflow.2003.11.005. <http://www.sciencedirect.com/science/article/pii/S0301932203002088>
- [44] Cho S, Dryer F. A numerical study of the unsteady burning behaviour of n-heptane droplets. *Combust Theory Model* 1999;3(2):267–80. doi:10.1088/1364-7830/3/2/004. <https://doi.org/10.1088/1364-7830/3/2/004>
- [45] Stauch R, Lipp S, Maas U. Detailed numerical simulations of the autoignition of single n-heptane droplets in air. *Combust Flame* 2006;145(3):533–42. doi:10.1016/j.combustflame.2005.12.013. <http://www.sciencedirect.com/science/article/pii/S0010218006000125>
- [46] Wang Y, Rutland C. Direct numerical simulation of ignition in turbulent n-heptane liquid-fuel spray jets. *Combust Flame* 2007;149(4):353–65. doi:10.1016/j.combustflame.2007.03.005. <http://www.sciencedirect.com/science/article/pii/S0010218007000697>
- [47] Awasthi I, Pope DN, Gogos G. Effects of the ambient temperature and initial diameter in droplet combustion. *Combust Flame* 2014;161(7):1883–99. doi:10.1016/j.combustflame.2014.01.001. <http://www.sciencedirect.com/science/article/pii/S0010218014000066>
- [48] Ashna M, Rahimian MH. LMB Simulation of head-on collision of evaporating and burning droplets in coalescence regime. *Int J Heat Mass Transfer* 2017;109:520–36. doi:10.1016/j.ijheatmasstransfer.2017.01.108. <http://www.sciencedirect.com/science/article/pii/S0017931016324309>
- [49] Stauch R, Maas U. The ignition of methanol droplets in a laminar convective environment. *Combust Flame* 2008;153(1):45–57. doi:10.1016/j.combustflame.2007.12.001. <http://www.sciencedirect.com/science/article/pii/S0010218008000023>
- [50] Awasthi I, Gogos G, Sundararajan T. Effects of size on combustion of isolated methanol droplets. *Combust Flame* 2013;160(9):1789–802. doi:10.1016/j.combustflame.2013.03.023. <http://www.sciencedirect.com/science/article/pii/S0010218013001119>
- [51] Turns S. An introduction to combustion: concepts and applications. New York: McGraw-Hill; 2000. <https://books.google.com.tr/books?id=sqVIPgAACAAJ>
- [52] Day MS, Bell JB. Numerical simulation of laminar reacting flows with complex chemistry. *Combust Theory Model* 2000;4(4):535–56. doi:10.1088/1364-7830/4/4/309. <https://doi.org/10.1088/1364-7830/4/4/309>
- [53] Cuoci A, Frassoldati A, Faravelli T, Ranzi E. Numerical modeling of laminar flames with detailed kinetics based on the operator-splitting method. *Energy Fuels* 2013a;27(12):7730–53. doi:10.1021/ef4016334. <https://doi.org/10.1021/ef4016334>
- [54] Cuoci A, Frassoldati A, Faravelli T, Ranzi E. A computational tool for the detailed kinetic modeling of laminar flames: application to  $C_2H_4/CH_4$  coflow flames. *Combust Flame* 2013b;160(5):870–86. doi:10.1016/j.combustflame.2013.01.011. <http://www.sciencedirect.com/science/article/pii/S0010218013000266>
- [55] Namara SM, Strang G. Operator splitting. Springer International Publishing; 2016. p. 95–114.
- [56] Kee R, Rupley F, Miller J. Chemkin-II: A fortran chemical kinetics package for the analysis of gas-phase chemical kinetics. 1989.
- [57] Kee RJ, Rupley FM, Meeks E, Miller JA. CHEMKIN-III: A FORTRAN chemical kinetics package for the analysis of gas-phase chemical and plasma kinetics. Sandia National Laboratories report SAND96-8216.
- [58] Jin Y, Shaw B. Computational modeling of n-heptane droplet combustion in air/diluent environments under reduced-gravity. *Int J Heat Mass Transfer* 2010;53(25):5782–91. doi:10.1016/j.ijheatmasstransfer.2010.08.005. <http://www.sciencedirect.com/science/article/pii/S0017931010004503>
- [59] Tryggvason G, Scardovelli R, Zaleski S. Direct numerical simulations of gas-liquid multiphase flows. Cambridge University Press; 2011.
- [60] Peskin CS. Numerical analysis of blood flow in the heart. *J Comput Phys* 1977;25(3):220–52. doi:10.1016/0021-9991(77)90100-0.
- [61] Leonard B. A stable and accurate convective modelling procedure based on quadratic upstream interpolation. *Comput Methods Appl Mech Eng* 1979;19(1):59–98. doi:10.1016/0045-7825(79)90034-3. <http://www.sciencedirect.com/science/article/pii/0045782579900343>
- [62] Chorin AJ. Numerical solution of the Navier-Stokes equations. *Math Comp* 1968;22:745–62.
- [63] Adams JC. MUDPACK: Multigrid portable fortran software for the efficient solution of linear elliptic partial differential equations. *Appl Math Comput* 1989;34(2):113–46. doi:10.1016/0096-3003(89)90010-6. <http://www.sciencedirect.com/science/article/pii/0096300389900106>
- [64] Udaykumar HS, Shyy W, Rao MM. ELAFINT: A mixed eulerian/lagrangian method for fluid flows with complex and moving boundaries. *Int J Numer Meth Fl* 1996;22(8):691–712. doi:10.1002/(SICI)1097-0363(19960430)22:8<691::AID-FLD371>3.0.CO;2-U.
- [65] Brown PN, Byrne GD, Hindmarsh AC. VODE: A variable-coefficient ode solver. *SIAM J Sci Stat Comput* 1989;10(5):1038–51. doi:10.1137/0910062. <https://doi.org/10.1137/0910062>
- [66] Borges R, Carmona M, Costa B, Don WS. An improved weighted essentially non-oscillatory scheme for hyperbolic conservation laws. *J Comput Phys* 2008;227(6):3191–211. doi:10.1016/j.jcp.2007.11.038.
- [67] Gibou F, Fedkiw RP, Cheng LT, Kang M. A second-order-accurate symmetric discretization of the poisson equation on irregular domains. *J Comput Phys* 2002;176(1):205–27. doi:10.1006/jcp.2001.6977.
- [68] Sato Y, Niceno B. A sharp-interface phase change model for a mass-conservative interface tracking method. *J Comput Phys* 2013;249:127–61. doi:10.1016/j.jcp.2013.04.035.
- [69] Muradoglu M, Tryggvason G. A front-tracking method for computation of interfacial flows with soluble surfactants. *J Comput Phys* 2008;227(4):2238–62. doi:10.1016/j.jcp.2007.10.003.
- [70] Muradoglu M, Tryggvason G. Simulations of soluble surfactants in 3d multiphase flow. *J Comput Phys* 2014;274:737–57. doi:10.1016/j.jcp.2014.06.024.
- [71] Han J, Tryggvason G. Secondary breakup of axisymmetric liquid drops. i. acceleration by a constant body force. *Phys Fluids* 1999;11(12):3650–67. doi:10.1063/1.870229. <https://doi.org/10.1063/1.870229>
- [72] Muradoglu M, Kayaalp AD. An auxiliary grid method for computations of multiphase flows in complex geometries. *J Comput Phys* 2006;214(2):858–77. doi:10.1016/j.jcp.2005.10.024. <http://www.sciencedirect.com/science/article/pii/S0021999105004766>
- [73] Williams G. Combustion theory. Addison-Wesley; 1985.
- [74] Yang JR, Wong SC. An experimental and theoretical study of the effects of heat conduction through the support fiber on the evaporation of a droplet in a weakly convective flow. *Int J Heat Mass Transfer* 2002;45(23):4589–98. doi:10.1016/S0017-9310(02)00164-3. <http://www.sciencedirect.com/science/article/pii/S0017931002001643>
- [75] Chauveau C, Birouk M, Gökalp I. An analysis of the d2-law departure during droplet evaporation in microgravity. *Int J Multiphase Flow* 2011;37(3):252–9. doi:10.1016/j.ijmultiphaseflow.2010.10.009. <http://www.sciencedirect.com/science/article/pii/S0301932210001886>
- [76] Hara H, Kumagai S. Experimental investigation of free droplet combustion under microgravity. *Proc Combust Inst* 1991;23(1):1605–10. doi:10.1016/S0082-0784(06)80432-7. Twenty-Third Symposium (International) on Combustion <http://www.sciencedirect.com/science/article/pii/S0082078406804327>

- [77] Jackson GS, Avedisian CT. The effect of initial diameter in spherically symmetric droplet combustion of sooting fuels. *Proc R Soc London Ser A Math Phys Eng Sci* 1994;446(1927):255–76. doi:10.1098/rspa.1994.0103. <http://rspa.royalsocietypublishing.org/content/446/1927/255>
- [78] Vieille B, Chauveau C, Chesneau X, Odeide A, Gökalp I. High-pressure droplet burning experiments in microgravity. *Proc Combust Inst* 1996;26(1):1259–65. doi:10.1016/S0082-0784(96)80343-2. <http://www.sciencedirect.com/science/article/pii/S0082078496803432>
- [79] Maroteaux F, Noel L. Development of a reduced n-heptane oxidation mechanism for HCCI combustion modeling. *Combust Flame* 2006;146(1):246–67. doi:10.1016/j.combustflame.2006.03.006. <http://www.sciencedirect.com/science/article/pii/S0010218006000903>